UC San Diego
UC San Diego Previously Published Works

Title

Mitochondrial Fission and Fusion Dynamics Generate Efficient, Robust, and Evenly Distributed Network Topologies in Budding Yeast Cells

Permalink

Journal

ISSN

Authors

Viana, Matheus P
Brown, Aidan I
Mueller, Irina A
et al.

Publication Date

DOI

Peer reviewed

Mitochondrial fission and fusion dynamics generate efficient, robust, and evenly distributed network topologies in budding yeast cells

Matheus P. Viana[1], Aidan I. Brown[2], Irina A. Mueller[1], Claire Goul[1], Elena F. Koslover[2], and Susanne M. Rafelski[1,3,§]

[1]*Developmental & Cell Biology and Center for Complex Biological Systems, UC Irvine, Irvine, CA 92697*

[2]*Department of Physics, University of California San Diego, La Jolla, CA 92093*

[3]*Biomedical Engineering, UC Irvine, Irvine, CA 92697*

Corresponding author and lead contact:

[§]Susanne Rafelski

2011 Biological Sciences III

Irvine, CA 92697

USA

949-824-4888

susanner@uci.edu

Currently at:

Susanne Rafelski

Allen Institute for Cell Science

615 Westlake Ave N

Seattle, WA 98109

USA

206-548-7070

susanner@alleninstitute.org

Current affiliations of other authors (if different form above):

Irina A. Mueller, Susanne M. Rafelski, Matheus P. Viana: Allen Institute for Cell Science, Seattle, WA 98109

Claire Goul: University of California, Berkeley, CA 94720

Summary

The simplest configuration of mitochondria in a cell is as small separate organellar units. Instead, mitochondria often form a dynamic, intricately connected network. A basic understanding of the topological properties of mitochondrial networks and their influence on cell function remains lacking. We performed an extensive quantitative analysis of mitochondrial network topology, extracting mitochondrial networks in 3D from live-cell microscopic images of budding yeast cells. In the presence of fission and fusion, mitochondrial network structures exhibited certain topological properties similar to other real-world spatial networks. Fission and fusion dynamics were required to efficiently distribute mitochondria throughout the cell and to generate highly interconnected networks that can facilitate efficient diffusive search processes. Thus, mitochondrial fission and fusion combine to regulate the underlying topology of mitochondrial networks, which may independently impact cell function.

Introduction

Mitochondria form dynamic, three-dimensional tubular networks in the cell. These structures range from many small individual organelles to one single large, continuous network depending on the organism, cell type, and functional state of the cell (Bereiter-Hahn, 1990). Mitochondrial networks are constantly remodeled by active and biologically

2

regulated fission and fusion events, which permit the connections between individual tubules to be formed and removed (Sesaki and Jensen, 1999; Jensen et al., 2000). Fission and fusion are implicated in maintaining mitochondrial DNA (mtDNA) integrity and mitochondrial network health by permitting damaged subregions of the network to either be restored, via content mixing with the rest of the network, or segregated and targeted for turnover (Twig and Shirihai, 2011; Hoitzing et al., 2015).

The wiring of a network impacts the behavior or performance of processes that take place within it, such as the speed with which a contagious disease can spread through a geographical area (Warren et al., 2002) or the efficiency of a transportation system (Lin and Ban, 2013). Complex networks research has developed measurements that formalize the topological properties of a network and assess network performance (Boccaletti et al., 2006). For example, the degree distribution of a network can modulate search times by random walks through the network, with nodes of a higher degree (more edges per node) being found more efficiently (Noh and Rieger, 2004). More highly interconnected networks are also more resilient to random failures, such as the disruption of generators in power-grid networks (Callaway et al., 2000; Boccaletti et al., 2006). Here we investigate whether well-established network properties are relevant for mitochondrial network structures.

A number of previous studies have focused on extracting and characterizing mitochondrial network structures (Zamponi et al., 2018; Harwig et al., 2018; Valente et al, 2017; Vowinckel et al., 2015; Leonard et al., 2015; Ahmad et al., 2013; Sokhorukov et al., 2012; Jakobs et al., 2003). Some of these studies obtained a large number of structures, allowing the compilation of statistics on network anisotropy, cluster fragmentation, and branch lengths (Zamponi et al., 2018; Valente et al, 2017; Vowinckel et al., 2015).

However, a comprehensive data-driven analysis of how fission and fusion dynamics modulate mitochondrial network properties has not previously been carried out.

We performed an extensive quantitative analysis of the underlying properties that characterize mitochondrial networks using the budding yeast, *Saccharomyces cerevisiae*, as a model system. To understand the contribution of mitochondrial dynamics to network topology, we analyzed *Δdnm1Δfzo1* fission/fusion mutant yeast cells that lack both the fission protein, Dnm1, and fusion protein, Fzo1 (Sesaki and Jensen, 1999; Jensen et al., 2000; Osman et al., 2015). We found that in the absence of fission and fusion dynamics, mitochondrial networks display severe topological and geometrical alterations. These alterations, in turn, impact mitochondrial distribution within the cell and expected transport efficiency within the mitochondrial network.

Results

Fission and fusion dynamics generate mitochondrial networks that are well distributed throughout the cell

Mitochondria cannot be created *de novo.* Therefore, some mitochondria must be actively transferred from mother to daughter cells. In budding yeast, mitochondria are moved from the mother to daughter cell along polarized actin cables that form along the mother-daughter axis during bud growth (Frederick and Shaw, 2007). The overall timescale of net mitochondrial transfer into the bud (via transport and retention mechanisms) is similar to the timescale of active polarized bud growth (Rafelski et al., 2012). Rapidly growing cells thus require continual transfer of mitochondria into the bud along these actin tracks.

4

To remove the confounding effect of polarized transport, we developed an experimental setup that permits yeast cells to transition from rapid, polarized growth to a non-polarized, non-dividing steady state. Yeast cells grown under physical constraints arrest as unbudded, non-dividing cells in the G2-M phase of the cell cycle (Suzuki et al., 2004). We grew yeast cells containing mitochondrial matrix-targeted fluorescent protein (mito-dsRed) in microfluidic chambers that trap the cells in a single monolayer. As the cell density in these chambers increases, the cells exert physical constraints on each other and transition from rapid, polarized growth to a non-polarized, non-dividing steady state over time. These cells continue to receive nutrient-rich media while in the microfluidic chambers. We observed a dramatic drop in the proportion of dividing cells (budding index) over time; by 24 hrs of growth in the microfluidic device only 6% of cells displayed buds (Figure 1A). 3D live-cell spinning-disk confocal microscopy confirmed that *Δdnm1Δfzo1* mitochondrial networks were collapsed and poorly distributed throughout the cell during rapid growth conditions (Figure 1B). After 24 hrs of growth, however, mitochondrial networks in *Δdnm1Δfzo1* cells looked well distributed and almost indistinguishable from wild-type cells (Figure 1C). This experimental setup thus permits us to investigate differences in the properties of mitochondrial networks independently of the effects of rapid polarized growth in a system where the network has the opportunity to reach a steady state.

Mitochondria are networks embedded in space, meaning their tubule ends and branch points (nodes) have a physical location in the cell. Mitochondrial networks thus fall into the class of geographical networks, as opposed to purely topological networks such as the World Wide Web, where hyperlink connections are generally independent of the physical locations where webpage nodes are hosted. It is well known that the way geographical networks are distributed in space has crucial implications to their function and performance (Hitchcock et al., 1996; Gastner and Newman, 2006). For example, slime

5

mold plasmodium veins are geographical networks with a high surface coverage that spans much of the available space to optimize their search for food. In another example, the larger the area covered by a transportation subway network, the greater the network capacity, in this case the subway ridership (Louf and Barthelemy, 2014).

To quantify the spatial distribution of mitochondria within each cell, we project the experimental mitochondrial network (Figure 1D) onto the surface of an ellipsoid (Figure 1E) and smooth out the network skeleton (Figure 1F) to generate a spatial probability distribution. The entropy of the probability distribution measures the degree to which mitochondria are uniformly distributed in the cell (see STAR methods). This evaluation of mitochondrial spatial distribution is shown for a more evenly distributed example in Figures 1D-F and a less evenly distributed example in Figures 1I-K.

To enable comparison between the *in vivo* mitochondrial distributions and a passive process, we simulated spatially-embedded random walks along the ellipsoid surface and calculated the entropy values corresponding to their distributions (Figures 1G-H and L-M). These random walks serve as a null model, representing randomly sampled configurations of a single long filament with persistence length corresponding to the measured value for mitochondrial tubules (see STAR methods for details). We note that such random walk structures are expected to arise from mitochondrial growth through the biogenesis and insertion of new mitochondrial material, which would lengthen network edges without altering the connectivity.

Figure 1N shows the distribution entropy for wild-type, *Δdnm1Δfzo1*, and simulated null model (random walks) – greater entropy represents networks that occupy the available space more uniformly. *In vivo* networks (wild-type and *Δdnm1Δfzo1*) are substantially

more uniformly distributed than the null model, and wild-type networks are on average more uniformly distributed than *Δdnm1Δfzo1* networks lacking fission and fusion. We note that increasing the total length of the mitochondrial network necessarily increases the occupied area of the cell surface and thus the entropy of the distribution. However, for both wild-type and *Δdnm1Δfzo1* mutant networks this increase is much steeper than for the null model. This suggests that, as more mitochondria are produced, they spread through space via a basal mechanism common to both wild-type and *Δdnm1Δfzo1* cells yet distinct from a purely passive random extension over the surface that does not account for branching or self-avoidance.

To more directly characterize the spatial spreading of networks beyond what would be expected for the null model of a single growing filament, we normalized the experimental spatial distribution entropies. The entropy of each *in vivo* mitochondrial network was divided by the typical spatial distribution entropy achieved by the null model. We found that the normalized spatial distribution of mitochondria in wild-type cells does not change significantly as the cells transition from rapid polarized growth to steady state over time in the microfluidic chambers (Figures 1O and P). In the absence of fission and fusion however, rapidly growing, polarized *Δdnm1Δfzo1* cells display a significantly decreased normalized spatial distribution within the cell, which is only partially recovered when the cells transition to steady state (Figures 1O and P). These results suggest that a fission/fusion-dependent mechanism for distribution complements the basal distribution mechanism and guarantees that wild-type cells always display a well-distributed mitochondrial network independently of polarized growth and at all stages of the cell cycle (Figure 1Q).

Fission and fusion dynamics generate more highly interconnected mitochondrial network topologies

Mitochondrial networks in *Δdnm1Δfzo1* cells have previously been reported to visually mostly resemble wild-type networks, even in rapidly growing conditions, with relatively minor differences compared to the dramatic over-fused or over-fragmented networks seen in the single fission or fusion mutants (Sesaki and Jensen, 1999; Jensen et al., 2000; Osman et al., 2015). We wondered whether these apparent similarities held true at the level of network topology or whether mutant cells exhibited similar spatial distributions of mitochondria but with underlying differences in the connectivity of these networks. We skeletonized mitochondrial networks of non-dividing steady state cells in 3D using MitoGraph v2.0 software. MitoGraph v2.0 has previously been validated for measuring mitochondrial content (Viana et al., 2015). We applied MitoGraph v2.0 software to extract "Mitochondrial Graph" representations (referred to as MitoGraphs; Rafelski et al., 2012). In MitoGraphs the mitochondrial tubules represent the edges and the tubule ends and branch-points represent the nodes of the network (Figures 2A-C).

We found that wild-type MitoGraphs are planar with respect to the cell surface, meaning that when the network is projected onto the cell surface, we do not observe any edges crossing over each other (Figures 2D-G). This planarity was fission/fusion-dependent; in *Δdnm1Δfzo1* cells we observed that about 20% of mitochondrial tubules were capable of detaching from the inner periphery of the cell and overlapping another mitochondrial tubule. The loss of mitochondrial network planarity is consistent with the idea that processes and proteins involved with mitochondrial localization through tethering are interdependent with those regulating mitochondrial fission and fusion (Cerveny et al., 2007; Lackner et al., 2013; Pernice et al., 2016), aligning with a similar relationship found in mammalian cells (Katajisto et al., 2015).

Visual comparison of MitoGraphs (Figures 2H-I) revealed an obvious difference in the connectivity pattern between wild-type and *Δdnm1Δfzo1* mitochondrial networks. Fission/fusion defective networks appeared much less branched than wild-type networks. The formation of a new branch occurs primarily through a fusion event at a location where two tubules come into contact with each other (Nunnari et al., 1997) and secondarily through the pulling out of a new tubule from an existing one (~four-fold less frequent, N=7; data not shown) (Osman et al., 2015). We would thus expect that wild-type cells with a greater density of mitochondrial tubules at the surface would have a higher chance of two tubules coming into contact and exhibit more highly interconnected networks. In contrast, fission/fusion defective networks, generated by growth and branching only, would lose this connectivity dependence on density.

We measured the number of neighbor nodes per node (degree) in each network to evaluate the connectivity of MitoGraphs. The average degree has been linked to several important aspects of network function. For instance, a more connected network (higher average degree) is better able to maintain flow after losing a random edge (Katifori et al., 2010). We found a strong correlation (R = 0.64 and p-value<2.2×10^{-16}) between the average degree and the mitochondria-to-cell surface ratio in wild-type cells, which is much weaker in fission/fusion mutant cells (R = 0.27 and p-value<0.051; Figure 2J). These results are consistent with a dominant role for fusion as a key process controlling network connectivity.

We next applied a series of standard measurements used in the networks field to quantify and formalize the differences in topological properties between wild-type and *Δdnm1Δfzo1* mitochondrial networks (Table 1). Some of these properties have been studied before for

mammalian mitochondrial networks (Sukhorukov et al., 2012) and other biological networks, such as slime mold plasmodium veins (Baumgarten et al., 2010) and plant leaf venations (Katifori et al., 2010). These studies have shown that, due to spatial constraints, each node in a real-world geographical network can only have a limited number of connections (Sukhorukov et al., 2012; Mark et al., 2008; Perna et al., 2011; Fessel et al., 2012). Consequently the distribution of node connectivities (degrees) in such networks is heavily biased to small values. We found that MitoGraphs exist at the extreme of degree distributions, with networks consisting almost entirely of nodes of degrees 1 and 3 (Figure 2K) and that MitoGraphs of *Δdnm1Δfzo1* cells are less interconnected than wild-type networks (Figure 2K). In fact, the average degree of *Δdnm1Δfzo1* MitoGraphs is below 2 (Figure 2J inset), which is typical of a class of "tree-like networks" containing no loops (Barthélemy, 2011), consistent with the observed *Δdnm1Δfzo1* network structures (Figure 2I).

Wild-type cells contained a mean of four connected components, while *Δdnm1Δfzo1* cells had only two components (Table 1). We found the multiple connected components of *Δdnm1Δfzo1* cells to be a surprise, given that these mutant cells are devoid of any fission dynamics. However, we observed that cytokinesis is able to split mitochondrial tubules in time-lapse experiments capturing cell division, thus generating multiple connected components in the absence of active fission (Figure S3 and Movie S1). To ensure that the change in connectivity in the *Δdnm1Δfzo1*cells did not arise from a possible loss of respiratory function or mtDNA, we compared the number of connected components in mutant cells with defective respiration (*Δcox6* cells, e.g. rho⁻) or devoid of mtDNA (*Δmip1* cells, e.g. rho^0). We found that, contrary to the *Δdnm1Δfzo1* cells, which contain fewer connected components, the *Δcox6* and the *Δmip1* mutant cells contained either a similar number or more connected components than wild-type cells (Figure S4).

Previous work suggested that mitochondrial networks in mammalian cells are in a percolation regime, where a single network component contains a large proportion (~35%) of the mitochondrial content (Mark et al., 2008; Sukhorukov et al., 2012). Mitochondrial networks in wild-type budding yeast are in a highly connected state, with a mean of 90% of total mitochondrial content contained in a single connected component (Table 1). The largest component in *Δdnm1Δfzo1* cells contained a large proportion of mitochondrial content, with a mean of 78% (Table 1). These results highlight that mitochondrial networks in budding yeast are in a highly connected state, well above the percolation regime predicted in mammalian cells.

Another classic measure of network connectivity that has been linked to functional efficiency in biological networks is the presence and abundance of loops within the network. For instance, loops enhance the transport properties within networks of chambers inside termite nests (Perna et al., 2012; Mileyko et al., 2012), confer robustness against local damage in plant leaf venation networks, and are required for optimal transport in the presence of leaf nutrient flow fluctuations (Katifori et al., 2010; Corson, 2010). Similarly, the presence of loops could affect the spread of mitochondrial components, such as diffusive molecules, throughout the network. We measured loop abundance in MitoGraphs via two standard network measurements, the global and local redundancy of the network. Global redundancy is defined as the increased fraction of edges of a network compared to a tree with a similar number of nodes and connected components (STAR methods, Figure S5). We found that the global redundancy of wild-type MitoGraphs is similar to what is observed in other geographical networks (Figure S6), but that it is significantly decreased in fission/fusion mutant cells (Figure 2L). We also observed that mitochondria in wild-type cells display very specific types of small-sized

loops (typical size between 2 µm-6 µm; Figure S7). We quantified the abundance of these small-sized loops within MitoGraphs via the local redundancy index, the percentage of edges that belong to at least one of these small-sized loops (see STAR methods and Figure S5). *Δdnm1Δfzo1* MitoGraphs display very low redundancy compared to wild-type MitoGraphs (Figure 2M). Together, these standard network measurements quantitatively demonstrate that fission and fusion dynamics are required to generate more highly interconnected mitochondrial networks at both the local and global scale.

Fission and fusion dynamics generate mitochondrial networks that topologically resemble other real-world geographic networks

An underlying principle of real-world geographical networks is that the distance between nodes influences the overall network topology and thus topological and spatial properties are correlated in these networks. A well-known example is the scaling ($\ell \sim N^{-0.5}$) between the number of nodes and the average edge length in a geographical network, which is found in many different kinds of real-world networks including in man-made street or railway networks and in naturally occurring biological networks such as plant leaf venation or hyphae of the slime mold physarum (Louf and Barthelemy, 2014; Barthélemy, 2011). We found that wild-type mitochondrial networks display a dependence of edge length on node number that is consistent with the scaling relation for general real-world spatial networks (Figure 2N).

To confirm that this relationship between node number and edge length arises from distance-dependent node connectivity, we simulated mitochondrial networks with attributes similar to our experimental networks (STAR methods). In the simulated networks, *N* nodes are randomly positioned over the surface of a sphere of area *S*, and randomly interconnected with a distance dependent probability $P(\ell) \sim \exp(-\alpha\ell/\sqrt{\rho})$, where *ρ*

= *N/S* and α controls the strength of the distance dependence. We observed that simulated networks with α=2.5 exhibited a similar dependence of edge length on node number as observed for wild-type networks (Figure 2N inset). Mitochondrial networks are thus not purely random planar networks but instead exhibit a distance-dependent topology similar to other real-world geographic networks.

Fission/fusion mutant networks, however, have a notably steeper dependence of edge length on node number. The average edge length is ~two-fold longer than expected for a given number of nodes (Figure 2N, Table 1). These results suggest that fission and fusion are required to maintain well-established underlying scaling properties found in real-world geographic networks, including wild-type mitochondrial networks. The distinct relationship between node density and edge length for wild-type and *Δdnm1Δfzo1* networks in Figure 2N is further evidence of a structural difference between the two network types, setting *Δdnm1Δfzo1* networks apart from a wide variety of transportation networks.

Fission and fusion dynamics generate mitochondrial network topologies that can support improved spread throughout the network

The topological properties of real-world geographic networks are often linked to functional or performance improvements (Barthélemy, 2011). We hypothesized that wild-type mitochondrial networks might display improved functional properties compared to *Δdnm1Δfzo1* networks. The shortest path length is a standard metric used to quantify the relative performance of network transport-related tasks in real-world geographic networks (Mark et al., 2008; Estrada and Hatano, 2008; Latora and Marchiori, 2001). It measures the average shortest distance (number of edges) between all pairs of nodes. The shorter the path length is, the easier the communication between nodes. We measured the average shortest path length in the largest connected component of each MitoGraph and

normalized it by the size of the component. We found that this normalized shortest path length is drastically increased in the absence of fission and fusion (Figure 3A). A drawback of this measurement is that it is only applied to a single connected component. A more appropriate measurement that takes all connected components into account is the global efficiency. Larger values of global efficiency are associated with improved transportation efficiency, such as tunnel networks in ant colonies and street and subway networks (Latora and Marchiori, 2001; Buhl et al., 2006; Buhl et al., 2006b). Consistently, wild-type MitoGraphs had greater normalized global efficiency than fission/fusion mutant MitoGraphs (Figure 3B and STAR methods).

We hypothesized that the decreased normalized shortest path length and the increased normalized global efficiency confer functional advantages to wild-type mitochondrial networks. For instance, topological properties previously linked to improved transport-related performance could represent increased efficiency with which any diffusive process would spread throughout the network. We thus simulated the dynamics of diffusive particles within our experimentally measured MitoGraphs, treating edges as interconnected one-dimensional domains. Focusing on the largest connected component of each mitochondrial network, we determined the mean time for the first encounter between two simulated diffusing molecules that start uniformly distributed throughout the structure (Figure 3C). This metric approximates diffusion-limited reaction rates between molecules found at very low concentrations within the mitochondrial network structure. Encounter times are positively correlated with network total edge length, which effectively measures the volume of space that the molecules must explore to find each other. However, total edge length does not fully determine the average encounter time: for a given total edge length there is a broad spread of encounter times, with *Δdnm1Δfzo1* networks typically yielding larger encounter times than the wild-type structures.

To establish which structural features of the mutant network are responsible for the predicted increase in particle encounter kinetics, we also determined simulated encounter times on Bethe lattice structures - simplified tree networks with no loops, equal-length edges, and all nodes of degree 1 or 3 (Fig. 3C, inset). Bethe lattices with the mean wild-type edge length roughly corresponded to the longest encounter times for wild-type networks, suggesting loops (absent in Bethe lattices but present in most wild-type networks) decrease the search time. Bethe lattices with mean *Δdnm1Δfzo1* edge length had encounter times roughly matching the typical *Δdnm1Δfzo1* encounter times, consistent with the tree-like, nearly loop-less *Δdnm1Δfzo1* network structures. The comparison to Bethe lattice structures indicates that the increased individual edge length of the *Δdnm1Δfzo1* networks accounts for a small portion of the increased encounter times compared to wild-type networks. However, much of the difference stems from the distinction between tree-like *Δdnm1Δfzo1* networks and wild-type networks containing many loops.

The effect of loops on simulated diffusive search of mitochondrial network structures is shown by plotting the encounter time versus the cyclomatic number (or loop number), defined as (# edges) - (# nodes) + 1, which is closely related to the global redundancy. This metric counts the number of independent cycles (loops) in a graph structure (Derrible and Kennedy, 2011). In Figure 3D, simulated encounter times (color map) are plotted against loop number as well as total edge length, clearly showing decreased diffusive encounter times as loop number increases. Hence, the presence of loops in wild-type mitochondrial network structures is expected to enhance search times and reaction rates. It also appears that encounter time can be more narrowly specified with a combination of loop number and total edge length, compared to total edge length alone. Although wild-

type and *Δdnm1Δfzo1* networks have distinct typical encounter times for a given edge length (Figure 3C), networks with similar total edge length and loop number are seen to have very similar encounter times (Figure 3D). These results suggest that changes to loop number and total edge length account for most of the difference in simulated encounter times between wild-type and *Δdnm1Δfzo1* networks.

To explore the effect of network structure on molecular reaction rates, we also considered the simulated rate of arrival for diffusing molecules to a stationary target (placed at random within the network). This rate is dependent on the diffusive molecule concentration (Figure 3E, inset). In a two- or three-dimensional environment, diffusive arrival rates are expected to scale linearly with concentration, giving the usual kinetic behavior of reactions in bulk medium. In a one-dimensional environment, however, the rate of arrival scales with the square of concentration, resulting in distinct kinetics (Condamin et al., 2007). The mitochondrial structures interpolate between these two regimes, with high concentrations of molecules resulting in essentially one-dimensional kinetics that are the same for both wild-type and *Δdnm1Δfzo1* networks. Lower molecular concentrations approach two-dimensional behavior, with more rapid rates for wild-type network structures. The increased connectivity of wild-type networks is found to increase simulated reaction rates by up to 80% in the limit of very low molecular concentrations (Figure 3E). As the molecule concentration increases, the enhancement of search on wild-type over *Δdnm1Δfzo1* networks diminishes as the morphological difference between the two network types becomes unimportant for target search with dense molecular concentrations.

The results in Figure 3 suggest that the underlying network topology, generated by fission and fusion dynamics, can enhance efficient diffusive search throughout mitochondrial networks. This enhancement is expected to be particularly important for molecules that

exist with low copy numbers within the mitochondrial network structure. A large variety of proteins are present in mitochondria at low copy number (Morgenstern et al., 2017), such as intron splicing protein MNE1 (0.05-0.10 μm^{-1} for a typical 58 μm length mitochondrial network), mitochondrial degradosome component DSS1 (0.24-0.38 μm^{-1}), and mitochondrial RNA polymerase (0.55-1.24 μm^{-1}). The speed with which such proteins find their targets should be greatly accelerated by the high connectivity of wild-type mitochondrial networks.

Discussion

Intracellular structures comprise a wide range of geometries including physical network-like structures. It is well known that the way networks are wired impacts the transport processes that take place within them. We performed extensive quantitative analysis of the topological properties of the mitochondrial networks and the contribution of fission and fusion dynamics to these properties in *S. cerevisiae*. We took advantage of the small size of budding yeast to image entire mitochondrial networks. Our analysis reports a clear and consistent result that fission and fusion dynamics are required to generate underlying properties of the mitochondrial network that are predicted to be advantageous for the cell.

Our analysis revealed that wild-type mitochondrial networks display a very restricted degree distribution (Figure 2K) that could be a consequence of the limited types of biological events that can reshape the network (Sesaki and Jensen, 1999; Jensen et al., 2000, Sukhorukov et al., 2012). In addition, the topological properties of wild-type networks are consistent with those of other geographic (spatially constrained) networks found in nature and in man-made structures (Figure 2N). This suggests the possibility of some underlying functional advantage to this particular type of interconnected network

topology. In contrast, these properties were not maintained in the less connected, more tree-like mitochondrial networks seen in the absence of fission and fusion. Tree-like networks are known for being very fragile with respect to random failures (Katifori et al., 2010; Corson, 2010). These tree-like topologies are consistent with the idea that the only remaining topology-modifying events in these cells would be the pulling out of new branches and the splitting of the network via cytokinesis (which is no longer occurring in the steady state growth condition). Together, these results suggest that yeast cells lacking fission and fusion dynamics display mitochondrial networks that are less robust in maintaining network-wide transport properties compared to those found in wild-type cells as well as in a wide range of other real-world physical networks.

Efficient diffusive search within the mitochondrial networks is expected to be important for a number of biologically critical processes. Localized mitochondrial damage, for example due to intense ROS production, occurs very rapidly and its mitigation via mitochondrial content mixing requires both removal of damaged components away from the sites of damage as well as access of repairing components (e.g. chaperones, proteases) to these sites. Any damaged component constrained to travel within the membrane or matrix of the mitochondria (e.g. damaged membrane proteins or damaged lipids themselves) is expected to mix much more efficiently within a highly interconnected network. In addition, mitochondrial transcription and its regulation requires diffusive search by DNA-binding proteins present in low copy numbers within the mitochondrial lumen.

Our analysis was based solely on the underlying topology of the network that is generated as a consequence of fission and fusion dynamics. It did not take into account the action of active fission and fusion itself and how this may affect the spread of mitochondrial components throughout the network in addition to topological effects. Our results thus

suggest that in addition to considering the effects on content mixing that occur due to individual fusion events, one needs to also consider the topology of the network itself which generates underlying constraints to the system upon which active fission and fusion dynamics act.

Much of the work described here, including the topological characterization of network structures and quantification of diffusive search processes, could be readily applied to other intracellular network structures. One such structure is the extensively interconnected tubular network of the peripheral endoplasmic reticulum (ER) (Westrate et al., 2015). The peripheral ER shares many mitochondrial network features, including a looped structure, which spans much of the cell (Lin et al., 2014), dynamic reorganization (Georgiades et al., 2017), and a variety of distinct ER morphologies depending on cell type (Westrate et al., 2015). Further exploration of the parallels between these two networks could prove a fruitful future direction.

Author Contributions

M.P.V. and S.M.R. conceived and designed the study. I.A.M. and S.M.R. performed microscopy experiments and initial experimental data analyses. M.P.V. and C.G.

performed computational analyses. M.P.V. performed image processing. M.P.V., A.I.B. and E.F.K. performed modeling. M.P.V. and S.M.R. performed integrated data analysis and interpreted data. M.P.V., A.I.B., S.M.R. and E.F.K. wrote the manuscript with input from all authors.

Main Figure Legends

Figure 1: *Mitochondria are spatially less evenly distributed in fission/fusion defective cells.* **(A)** Budding index (percentage of cells with a bud) of wild-type and *Δdnm1Δfzo1* cells as a function of time grown in the microfluidic chamber. The solid black line represents a budding index of 6% and error bars are 95% confidence intervals. **(B)** Mitochondria in live, wild-type yeast cells in rapid growth conditions imaged with spinning disk confocal microscopy shown as the maximum intensity projection (MIP) of mitochondrial matrix-targeted dsRed. Left panels: wild-type cells. Right panels: fission/fusion mutant (*Δdnm1Δfzo1*) cells. **(C)** Same as (B) for non-polarized, non-dividing cells after 24 hrs in the microfluidic chamber under constant flow of glucose rich media. (**D-F and I-K**) The process of calculating the entropy of mitochondria of a cell for examples of cells with high and low values of spatial distribution, respectively. **(D and I)** To calculate the entropy of mitochondria of a given cell, we start with an experimental mitochondrial skeleton; **(E and J)** The skeleton is projected onto the ellipsoid that represents the cell surface; **(F and K)** The projected skeleton is convolved with a Gaussian kernel with SD=2.0 and normalized so that the values sum up to one and can be interpreted as a probability distribution. Finally we calculate the entropy of the resulting probability distribution (Eq. 1 in STAR methods). **(G-H and L-M)** Spatially-embedded random walks are used to simulate passively distributed networks and to normalize the entropy values obtained for each cell. **(N)** Entropy values as a function of mitochondrial density (length/area) for log-phase (0

hrs) wild-type (blue dots, one dot per cell) and *Δdnm1Δfzo1* cells (red dots, one dot per cell) grown in glucose. Black dots represent the entropy of simulated random walks for different density values. The green reference line was obtained by using local polynomial regression. **(O)** Examples of mitochondrial networks in yeast cells grown in glucose as a function of time in microfluidic chambers. Mitochondrial surfaces, generated by MitoGraph v2.0 software, are gold and cell surfaces are gray. Normalized spatial distribution values for each mitochondrial network are indicated beneath each cell. **(P)** Normalized spatial distribution of mitochondria in wild-type (blue, N=1268) and *Δdnm1Δfzo1* (red, N=1007) cells as the cells transition from log-phase (0 hrs) to steady state (72hrs). One dot per cell is plotted. Data points are spread out along the x-axis around each of the seven time points for visualization purposes. Large dots correspond to the mean values of each population. Dotted box represents the data used to generate panel Q. Green line represents the average normalized spatial distribution of mitochondria in simulations of passive diffusion. **(Q)** Normalized spatial distribution of mitochondria for different stages of cell cycle (as measured by bud volume) in polarized (log-phase; 0 hrs) cells grown in glucose. One dot per cell is plotted. Large dots correspond to the rolling average (centered within a 16 data point window size). Error bars are 95% confidence intervals.

Figure 2: *Mitochondrial networks display fission/fusion-dependent differences in their topological properties.* **(A)** Maximum intensity projection (MIP) of the top half of a matrix labeled mitochondrial network (mito-dsRed). **(B)** The top half of the respective MitoGraph with the cell surface in gray, the mitochondrial surface in gold, network edges in dark blue and network nodes as in light blue spheres. **(C)** Topological view of the MitoGraph shown in (B). Dark blue nodes correspond to nodes from the MitoGraph shown in (B). Translucent nodes in are not visible in (B) and dashed edges link translucent nodes to the rest of the network in the bottom half of the cell. **(D)** Projection of mitochondrial networks

onto the cell surface is planar in wild-type cells. **(E)** In the absence of fission and fusion we observed that the projection of mitochondrial networks onto the cell surface displays a large number of edges crossing over each other (e.g. green arrows). **(F)** Example of two edges crossing over each other as seen in the image stacks slices and the corresponding MIP. **(G)** Number of overlaps per edge in wild-type and *Δdnm1Δfzo*1 mutant cells. We verified that in absence of fission and fusion almost 20% of the edges detach from cell surface and overlap another edge. **(H)** MIPs of representative examples of matrix labeled mitochondria (dsRed) in wild-type cells and their respective network representations. **(I)** MIPs of representative examples of matrix labeled mitochondria (mito-dsRed) in *Δdnm1Δfzo1* cells and their respective network representations. **(J)** Average degree as a function of mitochondria-to-cell surface ratio (length of mitochondrial networks divided by cell surface area). Small blue and red data points represent experimental wild-type (N=350) and *Δdnm1Δfzo1* (N=50) cells, respectively (one dot per cell). Large points represent the rolling average. Inset corresponds to the average degree (# edges per node) of MitoGraphs in wild-type and *Δdnm1Δfzo1* cells. **(K)** Degree distribution of MitoGraphs in wild-type (N=350) and *Δdnm1Δfzo1* (N=50) cells. **(L)** Global redundancy (fraction of edges) of MitoGraphs in wild-type and *Δdnm1Δfzo1* cells. **(M)** Local redundancy (fraction of edges) of MitoGraphs in wild-type and *Δdnm1Δfzo1* cells. Error bars are 95% confidence intervals. **(N)** The average edge length of mitochondrial networks is normalized by the radius of a sphere with the same surface area as the cell. For the other 2D geographical networks, the normalization is the radius of a circle with the same perimeter as the network convex-hull (Figure S1). Small blue and red data points represent experimental mitochondrial networks in wild-type (N=350) and *Δdnm1Δfzo1* cells (N=50), respectively (one dot per cell). Linear regression analysis is shown in STAR methods. Large data points represent different examples of 2D geographical networks (Viana et al., 2013). Dashed black line represents $\sqrt{\pi/N}$, the average edge length expected for a

random network built by placing *N* points at random over the surface of a unit sphere and connecting them to their first neighbor. Inset shows data points of mitochondrial networks together with solid lines that represent the relationship obtained from the random model, discussed in STAR methods, for values of α = 0, 1.0 and 2.5. The solid lines represent the average of thousand simulations for each value of α. The 95% confidence intervals of the mean and the line thickness are about the same.

Figure 3: *Fusion and fission dynamics generate network topologies that can facilitate diffusive transport within the network*. **(A)** Average shortest path length of the largest connected component within wild-type (N=350) and *Δdnm1Δfzo1* (N=50) networks normalized by the component length. **(B)** Normalized global efficiency of mitochondrial networks in wild-type (WT) and *Δdnm1Δfzo1* cells. **(C)** Computed mean time for first encounter between two simulated particles diffusing on wild-type (blue circles) and *Δdnm1Δfzo1* (red circles) structures. Lines represent simulated diffusion on synthetic Bethe lattice tree networks with edge length matching the mean edge length of wild-type (1.29μm, orange-red) and *Δdnm1Δfzo1* (2.56μm, green) networks. Inset shows example Bethe lattice network. **(D)** Data from (C) plotted against the total edge length and the loop number of the network structures. Color represents encounter time in seconds. Wild-type are shown as dots and *Δdnm1Δfzo1* as stars. **(E)** Rate of arrival for simulated diffusive molecules to reach a stationary target within the mitochondrial networks, as a function of molecule concentrations. Rates averaged over wild-type and *Δdnm1Δfzo1* network structures are plotted in the inset, with comparison to concentration scaling behaviors expected for one-dimensional ($\sim C^2$) and two- or three-dimensional ($\sim C$) systems. Main figure shows ratio between wild-type and *Δdnm1Δfzo1* network averages, with error bars giving standard error of the mean.

Table 1: *Topological and geometrical differences between mitochondrial networks in wild-type and Δdnm1Δfzo1 cells.* We manually correct a subset of N=50 wild-type networks to account for tubule intersections, and Figure S2 shows that the networks automatically generated by MitoGraph are similar to the manually corrected counterparts. Errors are standard deviations. Wilcoxon rank sum test reports the significance of the difference between the subset of manually corrected wild-type networks and *Δdnm1Δfzo1* networks (N=50) used in the paper.

	Wild-type	Wild-type (manually corrected)	*Δdnm1Δfzo1*	p-value (Wilcoxon rank sum test)
Avg. degree	2.2 ± 0.3	2.2 ± 0.2	1.8 ± 0.3	3.36e-09
Proportion end nodes (Pk1)	(40 ± 13)%	(40 ± 11)%	(57 ± 13)%	3.88e-09
Proportion of bifurcation nodes (Pk3)	(54 ± 12)%	(58 ± 12)%	(42 ± 13)%	8.08e-09
Global redundancy	0.18 ± 0.07	0.17 ± 0.06	0.07 ± 0.07	2.00e-09
Local redundancy	0.3 ± 0.2	0.3 ± 0.2	0.04 ± 0.09	4.79e-14
Largest connected component	(90 ± 14)%	(92 ± 13)%	(78 ± 24)%	0.13
Avg. number of components	3.8 ± 2.3	3.7 ± 2.2	2.4 ± 1.4	0.0005
Avg. edge length	(1.3 ± 0.2)μm	(1.4 ± 0.2)μm	(2.9 ± 0.8)μm	3.2e-17
Normalized shortest path length	0.12 ± 0.04	0.12 ± 0.03	0.24 ± 0.09	9.24e-14
Normalized global efficiency	0.66 ± 0.2	0.63 ± 0.2	0.44 ± 0.2	1.60e-05

STAR Methods

LEAD CONTACT AND MATERIALS AVAILABILITY

Further information and requests for resources and reagents should be directed to and will be fulfilled by the Lead Contact, Susanne Rafelski (susanner@uci.edu).

EXPERIMENTAL MODEL AND SUBJECT DETAILS

Yeast strains

Standard yeast methods were used throughout this study. We used the *Saccharomyces cerevisiae* W303A wild-type strain SRY-1 expressing the 2-micron plasmid pVT100U-dsRed to constitutively label the mitochondrial matrix (formerly SMR-12 in Rafelski et al., 2012). *Δdnm1Δfzo1* strain (-his and -trp selection), a gift from Jodi Nunnari, was transformed with pVT100U-dsRed to generate strain SRY-45. *Δdnm1Δfzo1* cells were maintained on SC selection plates containing glycerol (2%) and ethanol (3%) as carbon source to avoid formation of petites. Wild-type cells were maintained on SC selection plates with glucose (2%) as carbon source.

Δcox6 (SRY-175) and *Δmip1* (SRY-174) strains were created by disrupting COX6 and MIP1 using the pFA6a-HIS3MX6 plasmid (Longtine et al., 1998). The HIS3 disruption cassette was amplified by PCR from the plasmid using cassette specific primers as described in Longtine et al. (underlined) with added homology arms for COX6 and MIP1 (italic), respectively:

ΔCOX6_F: 5'

GTAGCGGAGATAAACAGCCGAACAATTGTATTTGACACATAAACTAATAAATATACAACAATG<u>C</u>
<u>GGATCCCCGGGTTAATTAA</u>

ΔCOX6_R: 5'

AATCGTTTTACAAAATAAATACGAATCTTATTTCAAATTGAGGAATTTTCCACAA<u>GAATTCGAGC</u>
<u>TCGTTTAAAC</u>

ΔMIP1_F: 5'

TCTAAAGAAGAGGTCGAGATGGGGGATTATATGTAGTTGTTGAGCAACGAGGGACAAGTATG<u>C</u>
<u>GGATCCCCGGGTTAATTAA</u>

ΔMIP1_R: 5'

AATGTGCTGTATATATAAATACAAATGCGAAAGCTAATGCAGATTTTGCCTA<u>GAATTCGAGCTC</u>

<u>GTTTAAAC</u>

PCR product was cleaned up (QIAquick PCR Purification Kit, QIAGEN, Germantown, MD, USA)

and transformed into SRY-1 (W303A wild-type strain expressing pVT100U-dsRed plasmid) using

the lithium acetate method. Transformed cells were grown on SC–his selection plates containing

glucose. Disruption of COX6 and MIP1 was confirmed in yeast clones using PCR using two primer

sets. Primer set 1 contained forward primer specific to the 5' UTR of COX6 and MIP, respectively,

while the reverse primer was specific for the HIS3 disruption cassette, resulting in amplification

when COX6 and MIP1 were disrupted by the proper integration of the HIS3 disruption cassette.

COX6_F: 5' AGCTTTCTTT GAATCTCCCTATGA

MIP1_F: 5' GCCTGTTCTG TGCCTCTT

HIS3_R: 5' CTCTTCAGGTAAGGGAGCTTTG

Primer set 2 contained same forward primers as primer set 1 but the reverse primer localized

within the COX6 and MIP1 gene, respectively, resulting in amplification when COX6 and MIP were

still intact.

COX6_R: 5' TACTTGGATGAATTGAAGGATGTCA

MIP1_R: 5' AAAAGAAACCATCACAAGCAAGAAC

Loss of COX6 and MIP1 was also confirmed by the lack of grow of yeast clones on SC-his

selection plates containing glycerol, suggesting that cells lost respiratory capacity. Actin cables

(Figure S9B) were visualized by transforming SRY-1 with an integration plasmid carrying ABP140-

3xGFP, a gift from David Drubin (pBS-3GFP-His3 + ABP140(-ORFnt1501-1884) +

ABP140(340bp_downstream; Toshima et al., 2006) to generate strain SRY-4.

METHOD DETAILS

Experimental setup

<u>Microfluidic device and microscope</u>

Wild-type and *Δdnm1Δfzo1* cells were grown overnight at 30°C in YP media with 2% glucose then

diluted and allowed to grow to early mid-log phase (O.D.$_{600}$ = 0.45 ± 0.04). Cells were appropriately

diluted and briefly vortexed, then loaded into the microfluidic CellAsic ONIX plates (Y04C-02, EMD Millipore, Billerica, MA, USA) using the manual CellAsic ONIX Microfluidic System (EMD Millipore) at a pressure of 3-4 psi until desired cell densities were reached (Figure 1). Cell concentrations at loading took different growth rates into account to permit comparable increase in cell density during the experiment. Media flow was maintained at 3psi throughout the experiment using the automated CellAsic ONIX Microfluidic System (EMD Millipore). Wild-type and *Δdnm1Δfzo1* cells were kept at room temperature and imaged at 0, 6, 12, 18, and 24 hours. For imaging wild type, *Δcox6* and *Δmip1,* cells were grown overnight at 30°C in YPD media, diluted and grown to mid-log phase (O.D.600 = 0.55 ± 0.09). Diluted mid-log cells were loaded into the microfluidic CellAsic ONIX plates (Y04C-02, EMD Millipore, Billerica, MA, USA) using the manual CellAsic ONIX Microfluidic System (EMD Millipore). Cells were imaged as described (Viana et al., 2015) using an inverted Nikon Eclipse microscope (Nikon Inc, Melville, NY, USA) with a Yokagawa CSUX1 spinning-disk head (Tokyo, Japan) equipped with a Hamamatsu EMCCD camera (C9100-13, Shizuoka, Japan). A 100x 1.49 NA oil TIRF objective (Nikon Inc, Melville, NY, USA), a 1.5x tube lens, and a piezo z-stage were used to obtain an x, y pixel size of 56 nm with 200nm z-steps. Images were collected with 100ms exposures for each the fluorescent and bright field channels. Imaging was controlled using Micromanager open source software (Edelstein et al 2010).

Image Processing and Data Analysis

Budding index calculation

To calculate the budding index, maximum intensity projections (MIP) of 3D fluorescent images of the mitochondrial networks were used to determine the percentage of budding cells per frame for each cell type, condition and time point.

Generating mitochondrial networks with MitoGraph

Confocal z-stacks containing many cells in the field-of-view were used to determine unbudded, non-dividing mothers and daughters cells. We used ImageJ to draw a region of interest (ROI) around the mitochondria of each cell and then created a single-cell sub-stack. The outside region

of the ROI was filled with random Poisson noise to mimic the original stack background and avoid spurious segmentation in the next step.

We used the software MitoGraph v2.0 (Viana et al., 2015) with default parameters to skeletonize single cell 16 bit z-stacks of fluorescently labeled mitochondria with pixel size 56 nm and 200 nm z-spacing. MitoGraph creates a 3D surface model as well as a graph representation of mitochondria. MitoGraph exports 3D skeletons and surfaces of mitochondria as VTK (Visualization Toolkit) files and we used the software Paraview 4.0 to open and work with these files. MitoGraph also exports information regarding the network connectivity, e.g. nodes coordinates and connection list, as text files that were analyzed by custom routines written in C++ and R.

We further validated MitoGraph v2.0 for use in the analysis of mitochondrial network topology in wild-type budding yeast cells (96% and 91% correct numbers of nodes and edges, respectively compared to manual results; STAR methods, Table S1).

MitoGraph v2.0 software cannot currently resolve overlapping tubules, thus resulting in less accurate *Δdnm1Δfzo1* MitoGraphs. To overcome this problem, *Δdnm1Δfzo1* MitoGraphs (N=50) were manually inspected and corrected to generate the *Δdnm1Δfzo1* dataset. We also manually corrected a subset of wild-type cells (N=50), and found no effects on any of our results and conclusions (Figure S2).

Determining the cell surface location

Method A - Convex hull method: In yeast, mitochondrial tubules anchor to the cell cortex thanks to the tethering between the mitochondrial outer membrane and plasma membrane invaginations (Cerveny et al., 2007; Lackner et al., 2013; Pernice et al., 2016). We can therefore use the outer surface of the mitochondrial network to determine the surface of the cell. This method for inferring the cell surface is especially powerful and accurate for steady state cells in which mitochondria are spread all over the cell. We begin with the 3D surface model of mitochondria generated by MitoGraph (Figure S8A) and we calculate its corresponding convex hull (Figure S8B) using a custom routine written in C++. The convex hull is the smallest convex polygon that contains all the 3D meshwork points. Next, we use the points of the convex hull to fit a triaxial ellipsoid (Figure S8C). Figure S8D shows an overlay of the initial mitochondrial surface and the resulting ellipsoid

that represents the cell surface. Our routine exports the ellipsoid surface made of a meshwork of triangles as a VTK file (www.vtk.org). The number of triangles in the mesh was kept fixed and equal to 4800. The minor, mid and major axes of the ellipsoid are exported as a text file and used to compute the surface area and volume of the cell.

Method B - Manual tracing: Contrary to steady state cells, most yeast cells in log-phase do not display mitochondria spread throughout the cell, especially in the absence of fission and fusion. Therefore, the convex-hull method is not applicable for log-phase cells. For these cells, we started by creating a Standard Deviation (SD) projection (Figure S9A) of the bright field z-stacks in ImageJ (Image → Stacks → Z Project... → Standard Deviation). Next, we manually drew an ellipse (green line) to determine the surface of the cell in the 2D projection. We determined the optimum location for the ellipse as the one that minimizes the error between the 2D projection and the convex hull method in steady state cells. We found that the optimum location for the ellipse lies between the dark ring marked by dashed white line in Figure S9A and the bright spots pointed by purple arrows in the same figure. The 2D ellipse is shifted in the z-direction such that its center matches the z-slices that have an intensity inflection in the bright-field channel. To determine the inflection slice, we created an ellipsoidal ROI five pixels wider than the original manually drawn ellipsoid and then calculated the SD of pixel intensity inside the enlarged ROI for every slice of bright field z-stack. The inflection slice was defined as the slice for which the SD of pixel intensity was the lowest. ImageJ exports values of minor and major axes of the ellipse as well as its coordinates for the center of mass as a text file that serves as input to a custom routine written in C++. This routine rotates the ellipse along its major axis to create an ellipsoid that represents the cell surface and computes the surface area and volume of the cell.

Validation of the two methodologies for cell surface calculation

We used cells containing both the protein Abp140 labeled with GFP to highlight actin cables (Figure S9B) and mitochondria labeled with RFP (Figure S9C) to quantify the errors associated to the cell surface extraction. First, we applied MitoGraph to the actin cable channel z-stacks. Although our imaging system does not have enough resolution to resolve actin cables, we

observed that MitoGraph was able to separate the actin cable signal from the background. Next, we used the 3D surface generated for actin cables as input for the convex hull method for calculating the cell surface. Because the actin cables are well spread all over the cell as shown in Figure S9B, we believe that the combination of the 3D actin cable-based surface generated by MitoGraph and the convex-hull method produces a very accurate estimation for the cell surface. We used this surface as a ground-truth for validating the other cell surface extraction methods. We compared results from both methods A and B against this ground-truth for a set of N=18 wild-type cells grown in glucose for 24 hrs. For these cells, we calculate the minor, mid and major axes, the surface area and volume of the 3D ellipsoids. Figure S9D shows the values of these attributes obtained by methods A (red circles) and B (green circles). The x-axis represent the values obtained for the ground truth. We observed a strong linear correlation (R=0.96) between the data for both A and B methods and the ground-truth for all attributes. This result indicates that both methods are very consistent across cells of different sizes.

We found that results shown in Figures 1D-P and Figure 2N in the main text could change due to errors associated with the cell surface estimation. In Figures 1D-P the spatial distribution analysis depends on the cell surface. In Figure 2N the y-axis is normalized by the radius of the sphere over which the network is projected and this radius is calculated as by $R = \sqrt{(S/4\pi)}$, where S is the cell surface area. However, the strong correlations found in Figure S9D (R = 0.99 for method A and R = 0.98 for method B) shows that the entropy values used to calculate the spatial distribution shown in Figures 1D-P are very similar regardless the methodology used to estimate the cell surface. In addition, the average error of R for method A (red) is on the order of $\Delta R = \pm 0.4 \mu m^3$ according to Figure S9D. This is too small and would not affect the main conclusion of Figure 2N that is mitochondrial networks follow the same dependence as other real-world networks in a fission/fusion dependent manner.

Representing the mitochondrial network as a spatial probability distribution
The mitochondrial skeleton is projected onto the ellipsoid and discretized into a sequence of equally spaced points. To prevent the projection from having gaps, we ensure the distance

30

between consecutive points is smaller than the smallest distance between the center of mass of adjacent triangles that form the meshwork of the ellipsoid surface. Next, we label the mesh triangles that contain at least one skeleton point with "1". Mesh triangles that do not contain any skeleton point are labeled with "0" (Figure 1E). The labeled mesh is convolved with a Gaussian kernel with *SD = 2.0 pixels,* which creates two-dimensional tubes with diameters visually matching mitochondrial tubules (Figure 1F). The scalar values of the convolved mesh are normalized so that the values of all triangles sum up to 1. This process is exemplified in Figures 1D-F and I-K for a cell with high and low spatial distribution, respectively.

Representing a passive process as probability distribution

We used random walks to simulate a cell where mitochondria are distributed solely according to a passive process. We started by creating a random walk of length *L* over the surface of an ellipsoid of area *S* (Figures 1G and L). The random walk starts with a particle located in a randomly chosen surface mesh triangle. At each time step, the particle moves to another triangle chosen at random among all the triangles located at distance *r* from the previous one. The parameter *r* represents the persistence length of mitochondrial tubules, which was measured from our experimental networks. Our measurements indicate r = 0.37 μm with no significant difference between wild-type and fission/fusion mutant cells and no significant variation with time (data not shown). Mesh triangles visited by the particle at least once are labeled with 1. Triangles not visited by the particle are labeled with 0. The labeled mesh is convolved with a Gaussian kernel with *SD = 2.0 as above.* The scalar values of the convolved mesh are normalized so that the values of all triangles sum up to 1 (Figures 1H and M).

Entropy-based spatial distribution of mitochondria

We calculated the entropy given by Equation 1 for each cell from our dataset. The term p_i represents the probability value calculated as described above for the *i-th* triangle of the meshwork. Figure 1N shows the values of entropy of log-phase (0 hrs) wild-type (blue dots) and fission/fusion double mutant (red dots) cells grown in glucose (one point per cell).

$$Entropy = -\sum_{i=1}^{4800} p_i \, log(p_i)(1)$$

Next, we simulated random walks with length in the range of 20 μm to 2020 μm in intervals of 5 μm as described above. Fifty random walks were generated for each length on the surface of an ellipsoid of area 86 μm^2, which is the mean surface area of cells in our dataset. The chosen value of surface area combined with the range of length ensures that we cover all the possible values of mitochondrial density (length/surface area) observed in the experimental data. These results were robust against the particular choice of ellipsoid surface (data not shown). We next calculated the entropy of each simulated random walk as described above. Results are shown as black dots in Figure 1N. We used local polynomial regression to estimate a reference line (green line) for entropy versus density expected by the diffusion process. Finally, we calculated the normalized spatial distribution of mitochondria for each cell as the ratio between the cell and the diffusion process entropy. Examples of this calculation for cells with high and low normalized spatial distribution are shown in Figures 1F and H and Figures 1K and M, respectively. To assign a single number to each population, we defined the relative distribution as the mean value of the entropy ratio averaged over all the cells of a population. For instance, in Figure 1P we show the relative distribution for populations at different time points. The blue and red points inside the dashed box were obtained by averaging the entropy ratio of cells shown as blue and red dots in Figure 1N.

Normalized global efficiency

The global efficiency is described in the literature as

$E_{glob} = \frac{1}{N(N-1)}\sum_{i \neq j}\frac{1}{L_{i,j}}$,

where Li,j is the length of the shortest path connecting nodes I and j in a network with N nodes (Latora and Marchiori, 2001). The global efficiency as defined above, do not account for size effect. Therefore, a mitochondrial network could be more or less efficiency depending on the cell size and not only its morphology. To compensate for this effect, we normalize the global efficiency

by its counterpart, where the path between nodes I and j are given by the geodesic distance along the cell surface Di,j. Therefore the normalized global efficiency is then given by

$$E_{normglob} = \sum_{i \neq j} \frac{1}{L_{i,j}} / \sum_{i \neq j} \frac{1}{D_{i,j}}.$$

Random network models

The simplest model of a mitochondrial network is that of a completely random model, where nodes are positioned at random inside the cell and then randomly connected. However, this basic model would not represent a true random model of mitochondrial networks for several obvious reasons: i) mitochondria are located at the periphery of the cell; ii) mitochondrial networks are planar with respect to the cell surface; iii) only nodes with degree 1 and 3 are observed in experimental networks; iv) distance likely plays an important role in establishing connections. Here we describe our attempt to incorporate these factors as much as possible in a random model for mitochondrial networks.

The model requires a planarity test to ensure that new edges do not cross any of the previously existing edges. This test is quite time consuming since it has to be performed for every new candidate edge. In addition, the number of discarded edges increases as the number of existing edges increases. Efficient algorithms are known to perform this type of planarity test when the edges lie either on a 2D plane or on a spherical surface. The task of testing the planarity of edges becomes a prohibitive when edges lie on the surface of a tri-axial ellipsoid, such as the yeast cells surface. For this reason, we decided to project our mitochondrial networks onto the surface of spheres that preserve the surface area of the cell surface.

Mapping experimental mitochondrial networks into spherical surfaces: We begin with an experimental mitochondrial skeleton and the ellipsoid that represents the cell surface, as shown in Figure S10A. Each point of the mitochondrial skeleton is projected onto the closest point on the ellipsoid meshwork to generate the projected network (Figure S10B). Next, edges of the projected network are replaced with geodesics between the corresponding nodes to generate a geodesic

network (Figure S10C). The geodesic between two nodes i and j was approximated by the shortest path between these nodes calculated along the ellipsoid meshwork. Finally, the geodesic is projected onto the surface of a sphere with the same surface area as the initial ellipsoid (Figure S10D). Figure S10E (left three panels) shows the length of the edges before and after each step of the process for generating the spherical projection (one point per edge). Figure S10E (rightmost panel) shows the relationship between the edge length in the original experimental network and in the resulting spherical projection (one point per edge). The strong linear correlation (R= 0.9, p-value $< 2\times10^{-16}$) suggests that most edges are well represented by straight lines on the surface and the difference in length at each step is very small. We extended this analysis to the edges (N=195593) of all the cells used in this paper and the result is shown in Figure S10F as a contour plot. Red contour lines indicate that the data points are greatly concentrated around the identity line (cyan dashed line).

Random models generation: We begin with the spherical projection of an experimental mitochondrial network as shown in Figure S11A (and obtained as described above). We extract four network attributes: number of nodes (N), surface area (S), total length of the network (L) and number of end-points (p_1), as shown in Figure S11B. These attributes serve as the input to create an instance of a random planar geographic (RPG) model (Figure S11C). In this model, N nodes are randomly positioned over the surface of a sphere of area S and randomly interconnected with a distance dependent probability ($P(\ell) \sim \exp(-\alpha\ell/\sqrt{\rho})$), where $\rho = N/S$ and α controls the strength of the distance dependence). The resulting network can display nodes of degree zero and nodes with degree two. Because these classes of connectivity do not exist in experimental mitochondrial networks by definition, we removed any nodes with degree zero or two in the simulated networks (Figure S11D). The numerical implementation of the RPG model has an additional test that ensures the algorithm does not enter an infinite loop. For a consecutive number Nlog(N) of attempts of adding a new connection that fail due to the planarity test, one existing edge is chosen at random and deleted. In addition, we force the algorithm to start all over if N^2 edges are deleted. The algorithm for RPG instances generation was written in C++ and uses the igraph library to perform graph-related computations.

Quantification and statistical analysis

Linear regression of figure 2N

Results of linear regression analysis indicate that wild-type networks display a scaling similar to other (2D) geographical networks but different from *Δdnm1Δfzo1* networks: intercept = 1.45 and slope = -0.54; *Δdnm1Δfzo1*: intercept = 2.04 and slope = -0.62; the set of other 2D geographical networks: intercept = 1.27 and slope = -0.54. Analysis of variance indicates no significant difference between wild-type data and the other 2D geographical networks (t = -1.3 and adjusted p-value = 0.34 for the intercept and t = 0.11 and adjusted p-value = 1.0 for the slope). Analysis of variance indicates a significant difference between wild-type and *Δdnm1Δfzo1* data (t = 3.6 and adjusted p-value < 6.0×10^{-4} for the intercept and t = -1.5 and adjusted p-value = 0.24 for the slope). P-values have been adjusted by Bonferroni correction.

Diffusion in mitochondrial networks

Mitochondrial networks are represented as nodes connected by edges with a specified physical length. Diffusion is simulated on the largest connected component of mitochondrial networks from each cell. Simulation of diffusion along the network is accelerated using the analytical solutions for diffusion time distributions in a one-dimensional domain. This approach, which leverages propagator functions for geometrically simple subdomains in an event-driven algorithm, is analogous to prior work on Green's-function accelerated kinetics simulations (van Zon and Wolde 2005) and target search by DNA-binding proteins (Koslover et al., 2011).

For encounter times (Figures 3C and D), both particles are initiated at a random position on the network, weighted by edge length. Each particle then undergoes one-dimensional diffusion along the network edges. When at a node, a particle propagates a distance equal to the length of the shortest edge connected to the node, over a time interval sampled from known diffusion-time distributions (Redner, 2001), and randomly selecting an edge. When positioned along an edge, the particle propagates to one of the two connected nodes in a time sampled from known diffusion-time distributions and choosing a node according to known splitting probabilities (Redner, 2001).

When two particles are simultaneously found on the same edge, each of them propagates as if there was a node halfway between the two particles, preventing them from passing in the tube without an encounter. Particles are considered to have encountered one another when they come within a separation of 10nm. Encounter times in Figures 3C and D are averaged over 1000 encounters.

For stationary target search, both a particle and a target are randomly positioned on the network (again weighted by edge length). The particle undergoes a random walk until it is within 10 nm of the target, when the particle is considered to have found the target. A search time distribution is obtained by sampling 10000 independent encounter events. This distribution is converted into a single-particle survival probability $S_1(t)$, i.e. the probability that the target has not been found before a given time by one searching particle. The single-particle survival probability is converted to an *N*-particle survival probability, $S_N(t) = (S_1(t))^N$. The rate in the inset of Figure 3E is the inverse of the mean *N*-particle survival time

$$\text{rate} = \left[\int_0^\infty t \frac{\mathrm{d}S_n(t)}{\mathrm{d}t} \mathrm{d}t \right]^{-1}.$$

DATA AND CODE AVAILABILITY

The datasets and code generated during this study are available at Mendeley at this URL:

https://data.mendeley.com/datasets/nshn8hhd6d/1

Supplemental text, figures, legends and video

Supplemental text, figures, and legends are all contained in a comprehensive PDF.

Supplemental Movie S1: *Cytokinesis is capable of splitting mitochondrial tubules in two even in absence of fission and fusion dynamics.* Related to Figure 2.

Declaration of Interests

The authors declare no competing interests.

References

Ahmad, T., Aggarwal, K., Pattnaik, B., Mukherjee, S., Sethi, T., Tiwari, B.K., Kumar, M., Micheal, A., Mabalirajan, U., Ghosh, et al., (2013). Computational classification of mitochondrial shapes reflects stress and redox state. Cell death & disease, 4(1), 461-e461

Barthélemy, M., (2011). Spatial networks. Physics Reports, 499(1-3), 1-101

Baumgarten, W., Ueda, T. and Hauser, M.J., (2010). Plasmodial vein networks of the slime mold Physarum polycephalum form regular graphs. Physical Review E, 82(4), 046113

Bereiter-Hahn, J., (1990). Behavior of mitochondria in the living cell. In International review of cytology (Academic Press), pp. 1-63

Boccaletti, S., Latora, V., Moreno, Y., Chavez, M. and Hwang, D.U., (2006). Complex networks: Structure and dynamics. Physics reports, 424(4-5), 175-308

Buhl, J., Gautrais, J., Deneubourg, J.L., Kuntz, P. and Theraulaz, G., (2006). The growth and form of tunnelling networks in ants. Journal of theoretical biology, 243(3), 287-298

Buhl, J., Gautrais, J., Reeves, N., Solé, R.V., Valverde, S., Kuntz, P. and Theraulaz, G., (2006). Topological patterns in street networks of self-organized urban settlements. The European Physical Journal B-Condensed Matter and Complex Systems, 49(4), 513-522

Callaway, D.S., Newman, M.E., Strogatz, S.H. and Watts, D.J., (2000). Network robustness and fragility: Percolation on random graphs. Physical review letters, 85(25), 5468

Cerveny, K.L., Studer, S.L., Jensen, R.E. and Sesaki, H., (2007). Yeast mitochondrial division and distribution require the cortical num1 protein. Developmental cell, 12(3), 363-375

Condamin, S., Bénichou, O., Tejedor, V., Voituriez, R. and Klafter, J., (2007). First-passage times in complex scale-invariant media. Nature, 450(7166), 77-80

Corson, F., (2010). Fluctuations and redundancy in optimal transport networks. Physical Review Letters, 104(4), 048703

Derrible, S. and Kennedy, C., (2011). Applications of graph theory and network science to transit network design. Transport reviews, 31(4), 495-519

Edelstein, A.D., Tsuchida, M.A., Amodaj, N., Pinkard, H., Vale, R.D. and Stuurman, N., (2014). Advanced methods of microscope control using µManager software. Journal of biological methods, 1(2)

Estrada, E. and Hatano, N., (2008). Communicability in complex networks. Physical Review E, 77(3), 036111

Fessel, A., Oettmeier, C., Bernitt, E., Gauthier, N.C. and Döbereiner, H.G., (2012). Physarum polycephalum percolation as a paradigm for topological phase transitions in transportation networks. Physical Review Letters, 109(7), p.078103

Frederick, R.L. and Shaw, J.M., (2007). Moving mitochondria: establishing distribution of an essential organelle. Traffic, 8(12), 1668-1675

Gastner, M.T. and Newman, M.E., (2006). Shape and efficiency in spatial distribution networks. Journal of Statistical Mechanics: Theory and Experiment, 2006(01), P01015

Georgiades, P., Allan, V.J., Wright, G.D., Woodman, P.G., Udommai, P., Chung, M.A. and Waigh, T.A., (2017). The flexibility and dynamics of the tubules in the endoplasmic reticulum. Scientific reports, 7(1), 1-10

Harwig, M.C., Viana, M.P., Egner, J.M., Harwig, J.J., Widlansky, M.E., Rafelski, S.M. and Hill, R.B., (2018). Methods for imaging mammalian mitochondrial morphology: a prospective on MitoGraph. Analytical

biochemistry, 552, 81-99

Hitchcock, D., Glasbey, C.A. and Ritz, K., (1996). Image analysis of space-filling by networks: Application to a fungal mycelium. Biotechnology Techniques, 10(3), 205-210

Hoitzing, H., Johnston, I.G. and Jones, N.S., (2015). What is the function of mitochondrial networks? A theoretical assessment of hypotheses and proposal for future research. BioEssays, 37(6), 687-700

Jajoo, R., Jung, Y., Huh, D., Viana, M.P., Rafelski, S.M., Springer, M. and Paulsson, J., (2016). Accurate concentration control of mitochondria and nucleoids. Science, 351(6269), 169-172

Jakobs, S., Martini, N., Schauss, A.C., Egner, A., Westermann, B. and Hell, S.W., (2003). Spatial and temporal dynamics of budding yeast mitochondria lacking the division component Fis1p. Journal of Cell Science, 116(10), 2005-2014

Jensen, R.E., Aiken Hobbs, A.E., Cerveny, K.L. and Sesaki, H., (2000). Yeast mitochondrial dynamics: fusion, division, segregation, and shape. Microscopy research and technique, 51(6), 573-583

Katajisto, P., Döhla, J., Chaffer, C.L., Pentinmikko, N., Marjanovic, N., Iqbal, S., Zoncu, R., Chen, W., Weinberg, R.A. and Sabatini, D.M., (2015). Asymmetric apportioning of aged mitochondria between daughter cells is required for stemness. Science, 348(6232), 340-343

Katifori, E., Szöllősi, G.J. and Magnasco, M.O., (2010). Damage and fluctuations induce loops in optimal transport networks. Physical Review Letters, 104(4), 048704

Koslover, E.F., de la Rosa, M.A.D. and Spakowitz, A.J., (2011). Theoretical and computational modeling of target-site search kinetics in vitro and in vivo. Biophysical journal, 101(4), 856-865

Lackner, L.L., Ping, H., Graef, M., Murley, A. and Nunnari, J., (2013). Endoplasmic reticulum-associated mitochondria–cortex tether functions in the distribution and inheritance of mitochondria. Proceedings of the National Academy of Sciences, 110(6), E458-E467

Latora, V. and Marchiori, M., (2001). Efficient behavior of small-world networks. Physical review letters, 87(19), 198701

Leonard, A.P., Cameron, R.B., Speiser, J.L., Wolf, B.J., Peterson, Y.K., Schnellmann, R.G., Beeson, C.C. and Rohrer, B., (2015). Quantitative analysis of mitochondrial morphology and membrane potential in living cells using high-content imaging, machine learning, and morphological binning. Biochimica et Biophysica Acta (BBA)-Molecular Cell Research, 1853(2), 348-360

Lin, C., Zhang, Y., Sparkes, I. and Ashwin, P., (2014). Structure and dynamics of ER: minimal networks and biophysical constraints. Biophysical journal, 107(3), 763-772

Lin, J. and Ban, Y., (2013). Complex network topology of transportation systems. Transport reviews, 33(6), 658-685

Longtine, M.S., Mckenzie III, A., Demarini, D.J., Shah, N.G., Wach, A., Brachat, A., Philippsen, P. and Pringle, J.R., (1998). Additional modules for versatile and economical PCR- based gene deletion and modification in Saccharomyces cerevisiae. Yeast, 14(10), 953-961

Louf, R., Roth, C. and Barthelemy, M., (2014). Scaling in transportation networks. PLoS One, 9(7)

Fricker, M.D., Lee, J.A., Boddy, L. and Bebber, D.P., (2008). The interplay between structure and function in fungal networks. Topologica, 1(1), 004-004

Mileyko, Y., Edelsbrunner, H., Price, C.A. and Weitz, J.S., (2012). Hierarchical ordering of reticular networks. PLoS One, 7(6)

Morgenstern, M., Stiller, S.B., Lübbert, P., Peikert, C.D., Dannenmaier, S., Drepper, F., Weill, U., Höß, P., Feuerstein, R., Gebert, M., et al., (2017). Definition of a high-confidence mitochondrial proteome at quantitative scale. Cell reports, 19(13), 2836-2852

Noh, J.D. and Rieger, H., (2004). Random walks on complex networks. Physical review letters, 92(11),

Nunnari, J., Marshall, W.F., Straight, A., Murray, A., Sedat, J.W. and Walter, P., (1997). Mitochondrial transmission during mating in Saccharomyces cerevisiae is determined by mitochondrial fusion and fission and the intramitochondrial segregation of mitochondrial DNA. Molecular biology of the cell, 8(7), 1233-1242

Osman, C., Noriega, T.R., Okreglak, V., Fung, J.C. and Walter, P., (2015). Integrity of the yeast mitochondrial genome, but not its distribution and inheritance, relies on mitochondrial fission and fusion. Proceedings of the National Academy of Sciences, 112(9), E947-E956

Perna, A., Kuntz, P. and Douady, S., (2011). Characterization of spatial networklike patterns from junction geometry. Physical Review E, 83(6), 066106

Perna, A., Kuntz, P., Theraulaz, G. and Jost, C., (2012). From local growth to global optimization in insect built networks. In Biologically inspired networking and sensing: algorithms and architectures (pp. 132-144). IGI Global

Pernice, W.M., Vevea, J.D. and Pon, L.A., (2016). A role for Mfb1p in region-specific anchorage of high-functioning mitochondria and lifespan in Saccharomyces cerevisiae. Nature communications, 7(1), 1-12

Rafelski, S.M., Viana, M.P., Zhang, Y., Chan, Y.H.M., Thorn, K.S., Yam, P., Fung, J.C., Li, H., Costa, L.D.F. and Marshall, W.F., (2012). Mitochondrial network size scaling in budding yeast. Science, 338(6108), 822-824

Redner, S., (2001). A guide to first-passage processes (Cambridge University Press)

Sesaki, H. and Jensen, R.E., (1999). Division versus fusion: Dnm1p and Fzo1p antagonistically regulate mitochondrial shape. The Journal of cell biology, 147(4), 699-706

Sukhorukov, V.M., Dikov, D., Reichert, A.S. and Meyer-Hermann, M., (2012). Emergence of the mitochondrial reticulum from fission and fusion dynamics. PLoS computational biology, 8(10)

Suzuki, M., Asada, Y., Watanabe, D. and Ohya, Y., (2004). Cell shape and growth of budding yeast cells in restrictive microenvironments. Yeast, 21(12), 983-989

Toshima, J.Y., Toshima, J., Kaksonen, M., Martin, A.C., King, D.S. and Drubin, D.G., (2006). Spatial dynamics of receptor-mediated endocytic trafficking in budding yeast revealed by using fluorescent α-factor derivatives. Proceedings of the National Academy of Sciences, 103(15), 5793-5798.

Twig, G. and Shirihai, O.S., (2011). The interplay between mitochondrial dynamics and mitophagy. Antioxidants & redox signaling, 14(10), 1939-1951

Valente, A.J., Maddalena, L.A., Robb, E.L., Moradi, F. and Stuart, J.A., (2017). A simple ImageJ macro tool for analyzing mitochondrial network morphology in mammalian cell culture. Acta histochemica, 119(3), 315-326

van Zon, J.S. and Ten Wolde, P.R., (2005). Simulating biochemical networks at the particle level and in time and space: Green's function reaction dynamics. Physical review letters, 94(12), 128103

Viana, M.P., Strano, E., Bordin, P. and Barthelemy, M., (2013). The simplicity of planar networks. Scientific reports, 3, 3495

Viana, M.P., Lim, S. and Rafelski, S.M., (2015). Quantifying mitochondrial content in living cells. In Methods in cell biology, 125, 77-93

Vowinckel, J., Hartl, J., Butler, R. and Ralser, M., (2015). MitoLoc: A method for the simultaneous quantification of mitochondrial network morphology and membrane potential in single cells. Mitochondrion, 24, 77-86

Warren, C.P., Sander, L.M. and Sokolov, I.M., (2002). Geography in a scale-free network model. Physical Review E, 66(5), 056105

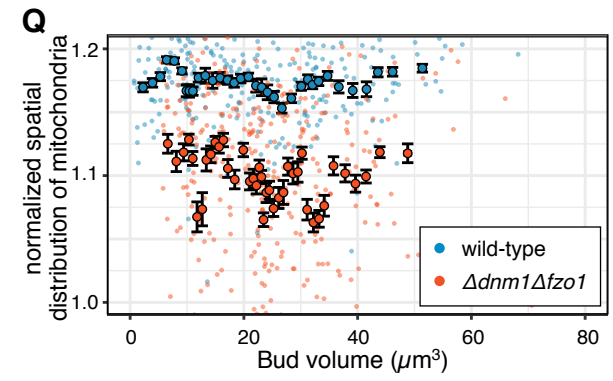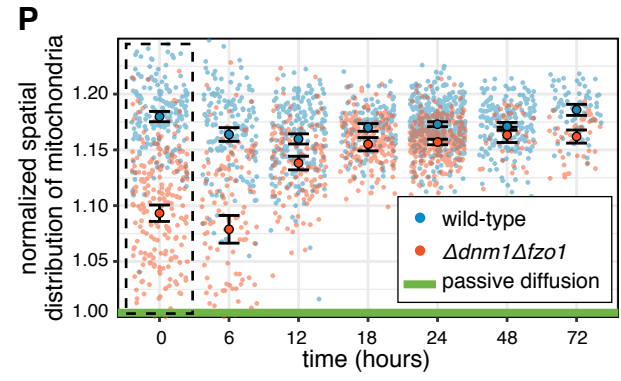Westrate, L.M., Lee, J.E., Prinz, W.A. and Voeltz, G.K., (2015). Form follows function: the importance of
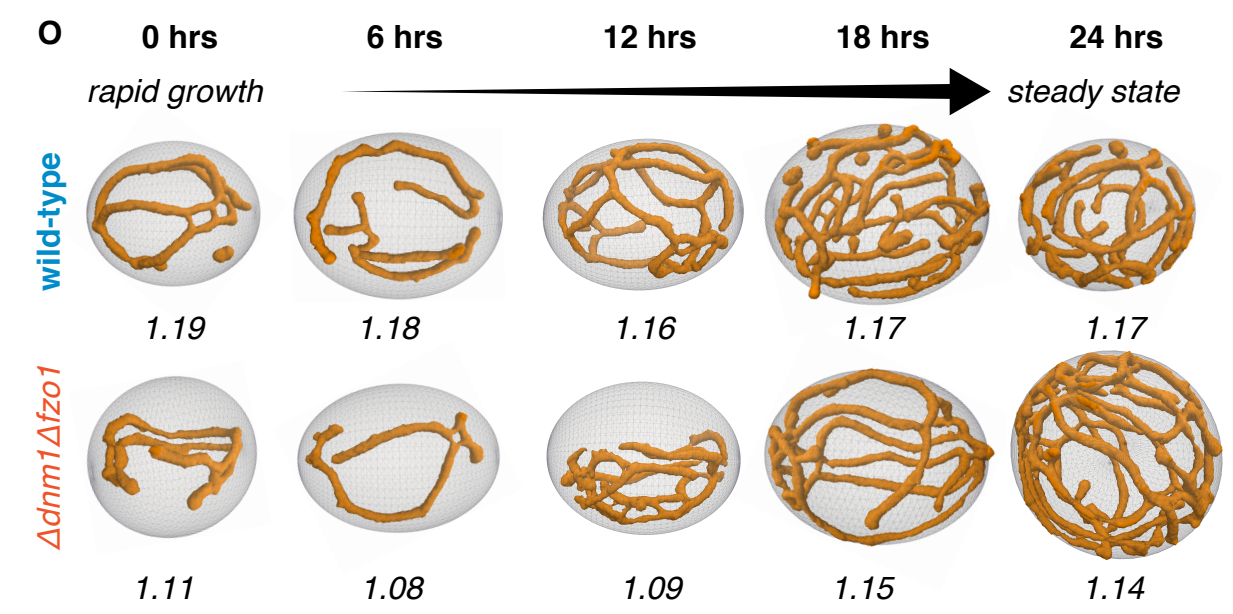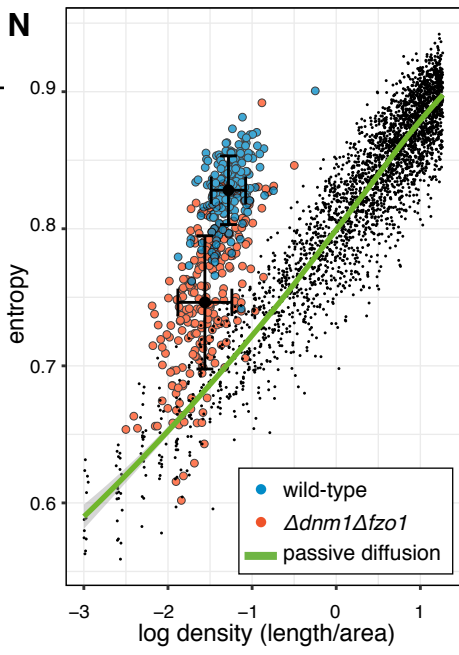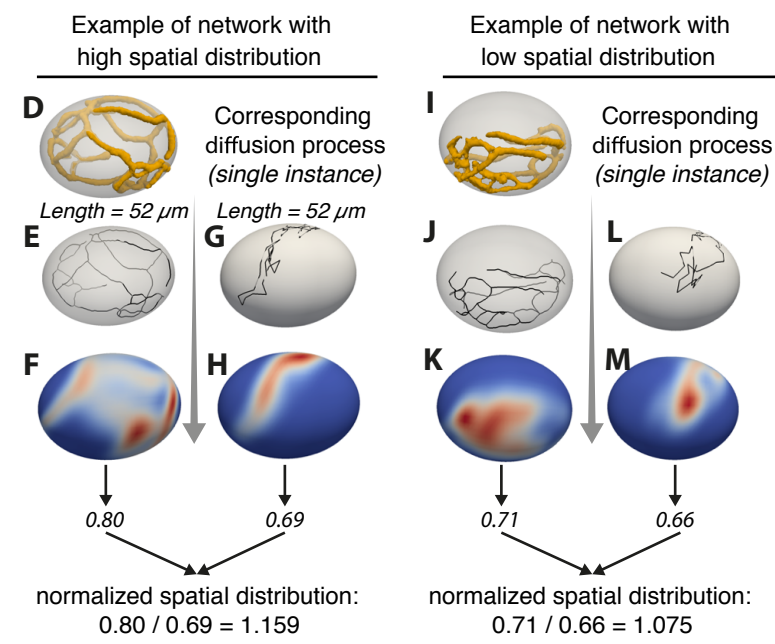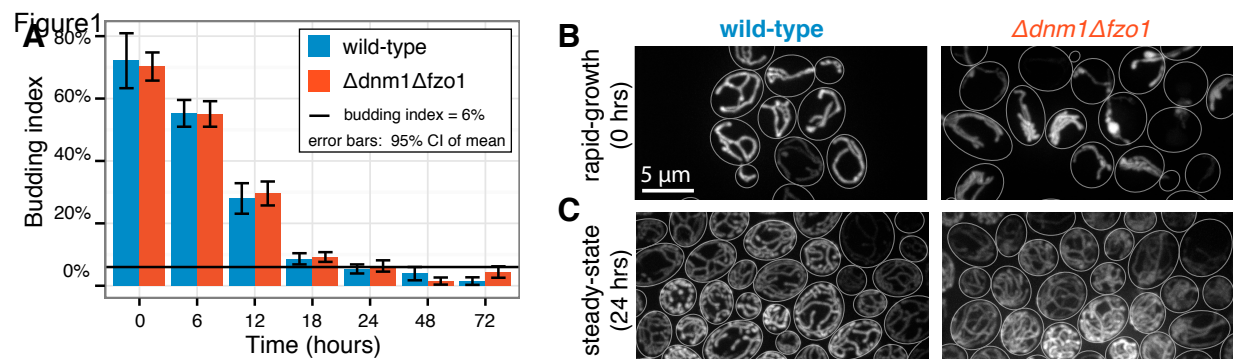
endoplasmic reticulum shape. Annual review of biochemistry, 84, 791-811

Zamponi, N., Zamponi, E., Cannas, S.A., Billoni, O.V., Helguera, P.R. and Chialvo, D.R., (2018). Mitochondrial network complexity emerges from fission/fusion dynamics. Scientific reports, 8(1), 1-10

KEY RESOURCES TABLE

REAGENT or RESOURCE	SOURCE	IDENTIFIER
Deposited Data		
Data and Code	This paper	https://data.mendeley.com/datasets/nshn8hhd6d/1
Experimental Models: Organisms/Strains		
SRY-1 strain (formerly SMR-12; W303A wild-type strain expressing pVT100U-dsRed plasmid)	Rafelski et al., 2012	N/A
Δdnm1Δfzo1 strain	Jodi Nunnari laboratory	N/A
SRY-45 strain (*Δdnm1Δfzo1* strain expressing pVT100U-dsRed plasmid)	This paper	
SRY175 (*Δcox6* in SMR12 strain)	This paper	N/A
SRY174 *(Δmip1* in SMR12 strain)	This paper	N/A
SRY-4 strain (SMR-12 expressing pABP140-3xGFP plasmid)	This paper	N/A
pVT100U-dsRed plasmid	Rafelski et al., 2012	N/A
pFA6a-HIS3MX6 plasmid	Wallace Marshall laboratory	N/A
pABP140-3xGFP plasmid	Toshima et al., 2006	N/A
Software and Algorithms		

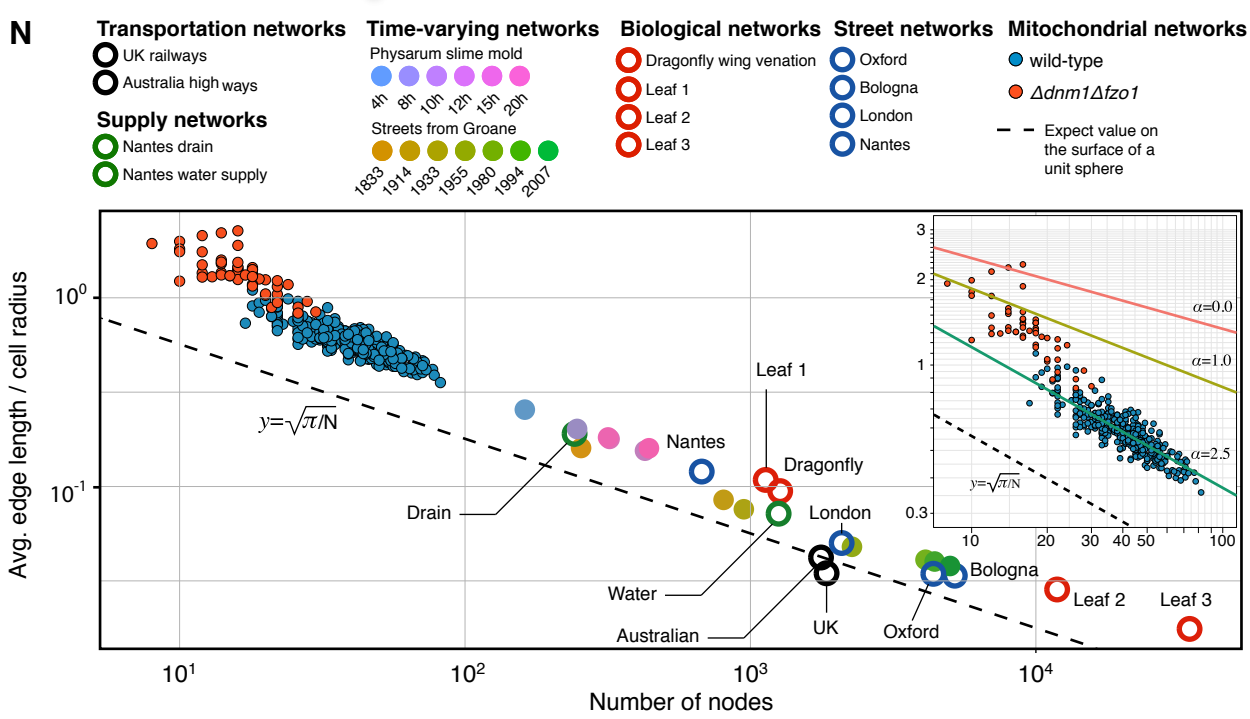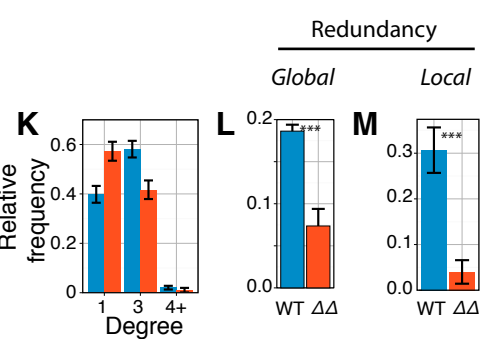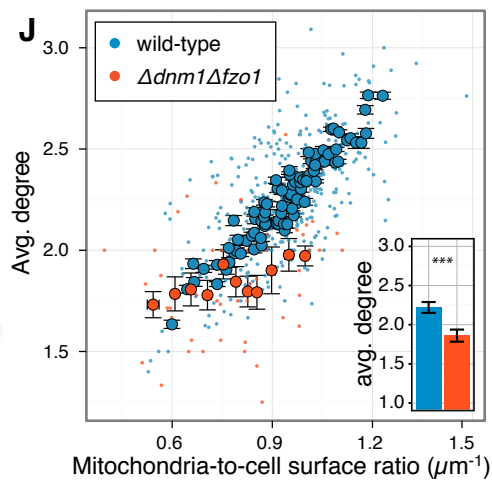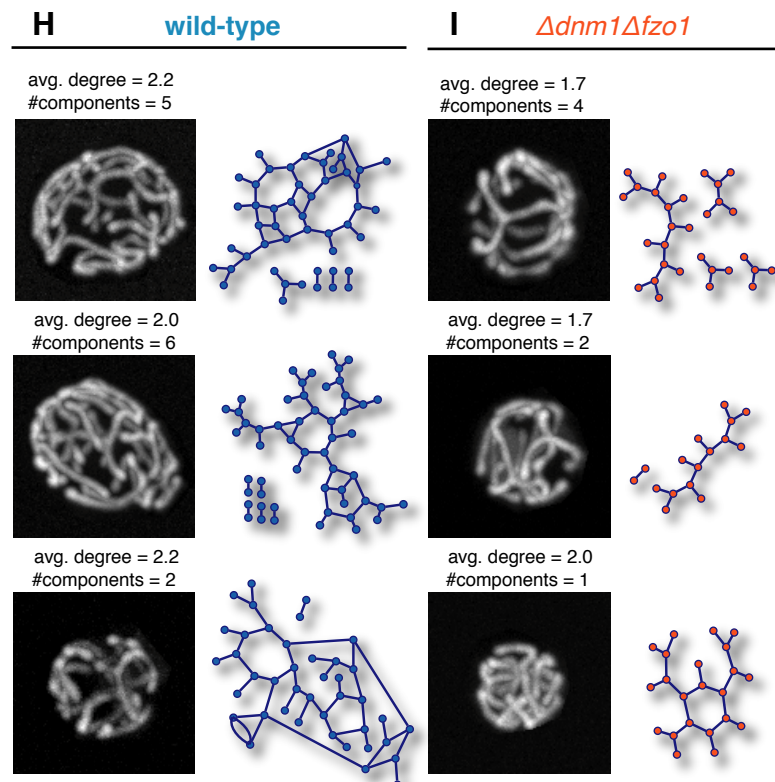|		
MitoGraph: software used for extracting the graph representation of mitochondrial networks from 3D zstcks of mitochondria-labeled cells	Viana et al., 2015	https://github.com/vianamp/MitoGraph
MitoDiffusion: C++ code for the calculation of entropy of mitochondrial networks as described in Figure 2	This paper	https://data.mendeley.com/datasets/nshn8hhd6d/1
LoopFinder: C++ code for counting number of loops in mitochondria networks via brute force search.	This paper	https://data.mendeley.com/datasets/nshn8hhd6d/1
MitoEfficiency: C++ code for calculating the normalized global efficiency of mitochondrial networks	This paper	https://data.mendeley.com/datasets/nshn8hhd6d/1
Algorithm for diffusive search on networks: this code uses simulations of diffusion on spatial networks to find mean encounter times between two diffusing particles, diffusive search times for stationary targets, and rates of finding stationary targets.	This paper	https://data.mendeley.com/datasets/nshn8hhd6d/1

Figure1

Figure2

A Mitochondria

B MitoGraph

C Network

D wild-type

E Δdnm1Δfzo1

F slice
25
26
27
28
29
MIP

G
- wild-type
- Δdnm1Δfzo1

mean = 0.4%
mean = 20%

Relative frequency

100 x #overlaps / #edges

H wild-type

avg. degree = 2.2
#components = 5

avg. degree = 2.0
#components = 6

avg. degree = 2.2
#components = 2

I Δdnm1Δfzo1

avg. degree = 1.7
#components = 4

avg. degree = 1.7
#components = 2

avg. degree = 2.0
#components = 1

J
- wild-type
- Δdnm1Δfzo1

Avg. degree

Mitochondria-to-cell surface ratio (μm^{-1})

avg. degree
***
WT ΔΔ

K
Relative frequency
Degree
1 3 4+

Redundancy

Global **L**
***
WT ΔΔ

Local **M**
***
WT ΔΔ

N

Transportation networks
- UK railways
- Australia high ways

Supply networks
- Nantes drain
- Nantes water supply

Time-varying networks
Physarum slime mold
4h 8h 10h 12h 15h 20h
Streets from Groane
1833 1914 1933 1955 1980 1994 2007

Biological networks
- Dragonfly wing venation
- Leaf 1
- Leaf 2
- Leaf 3

Street networks
- Oxford
- Bologna
- London
- Nantes

Mitochondrial networks
- wild-type
- Δdnm1Δfzo1
- - - Expect value on the surface of a unit sphere

Avg. edge length / cell radius

$y = \sqrt{\pi/N}$

Drain
Nantes
Leaf 1
Dragonfly
London
Water
Australian
UK
Oxford
Bologna
Leaf 2
Leaf 3

$\alpha = 0.0$
$\alpha = 1.0$
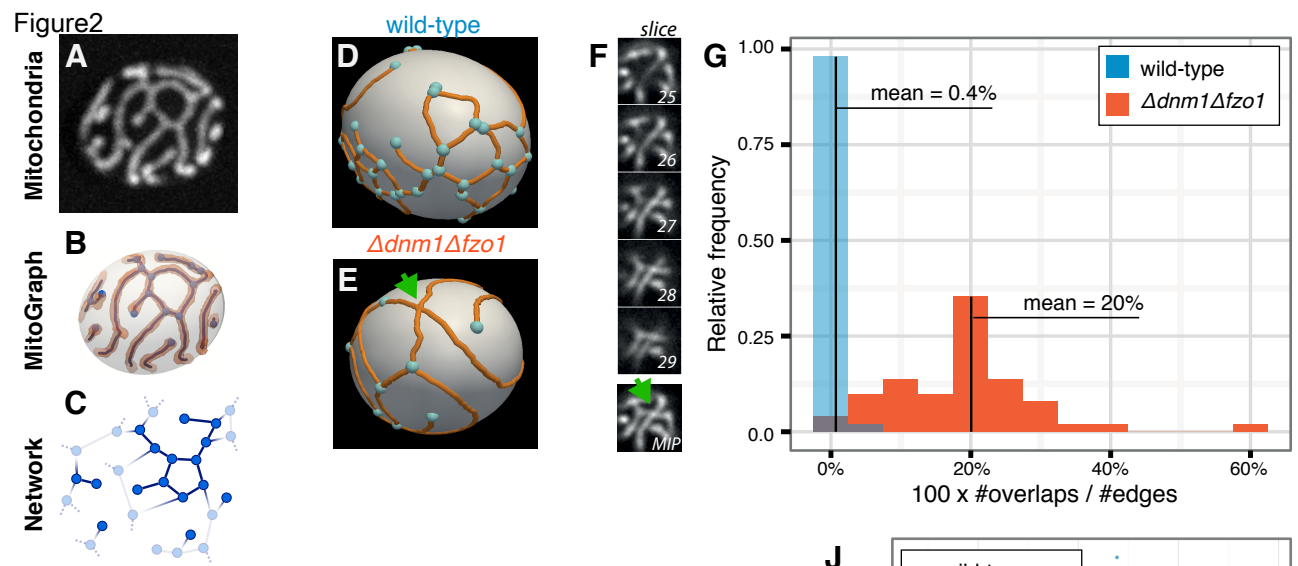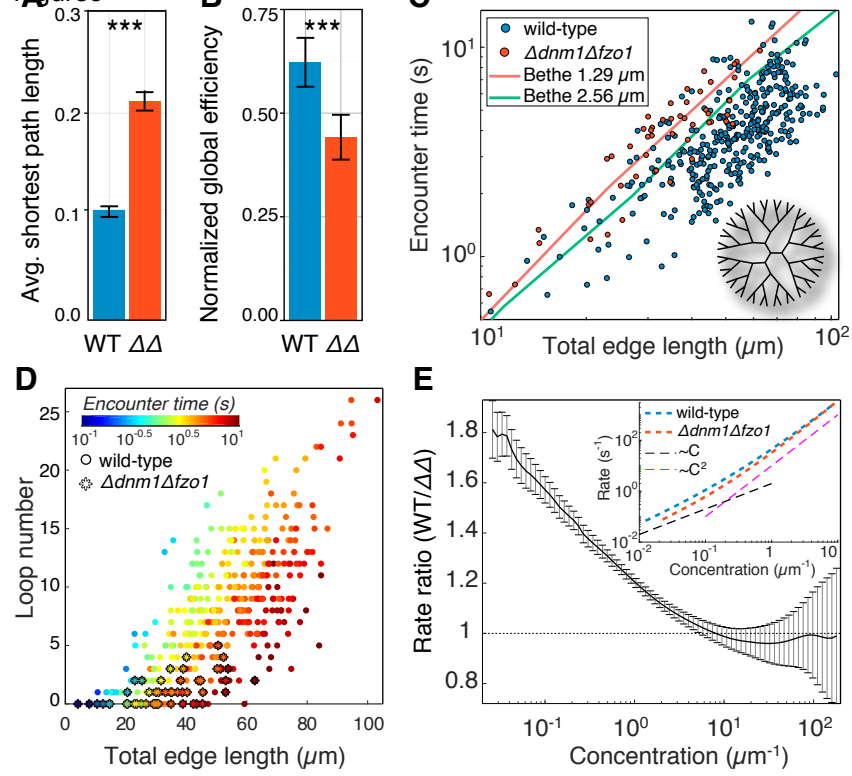$\alpha = 2.5$
$y = \sqrt{\pi/N}$

Number of nodes

Figure3

Supplemental information for "Mitochondrial fission and fusion dynamics generate efficient, robust, and evenly distributed network topologies in budding yeast cells"

Matheus P. Viana, Aidan I. Brown, Irina A. Mueller,

Claire Goul, Elena F. Koslover, and Susanne M. Rafelski

	Magnitude Error		Overall Error	
	Wild-type	**Δdnm1Δfzo1**	**Wild-type**	**Δdnm1Δfzo1**
# Nodes	5.81%	13.90%	3.90%	13.90%
# Edges	9.26%	22.90%	8.51%	22.90%
Avg. degree	4.95%	10.52%	4.83%	10.52%
Total length	2.67%	3.14%	0.97%	3.14%
Avg. edge length	9.71%	26.66%	-8.81%	-26.66%
SD edge length	18.43%	34.20%	-18.43%	-34.20%
# Connected components	17.50%	25.00%	-17.50%	-25.00%
Phi (size of largest connected component)	5.53%	1.78%	5.26%	1.78%

TABLE S1. *Average errors of measurements made by MitoGraph for wild-type and fission/fusion double mutant cells.* Related to Figure 2. N=50 skeletons of wild-type and N=50 skeletons of fission/fusion double mutant cells were manually corrected. For each cell, $error_i = 1 - \frac{Qr}{Qm}$, where Qr represents the quantity in the real skeleton and Qm represents the quantity in the manually corrected skeleton. Magnitude error was calculated as $MagError = \frac{100}{N} \sum_i^N |error_i|$ and overall error was calculated as $OveError = \frac{100}{N} \sum_i^N error_i$. This table demonstrates that Mitograph displays much poorer results for $\Delta dnm1 \Delta fzo1$ cells. This is mainly due to topological artifacts caused by overlapping tubules in $\Delta dnm1 \Delta fzo1$ networks.

	Rapid growth				Steady state
	0hs	**06hs**	**12hs**	**18hs**	**24hs**
Wild-type	434	352	269	176	350(50)
Δdnm1Δfzo1	509	340	228	251	260(50*)

TABLE S2. *Number of cells in each population of our dataset.* Related to Figure 2. Between parentheses we indicate the number of manually corrected skeletons. *Number of $\Delta dnm1 \Delta fzo1$ skeletons used in the main text for topology-related studies.
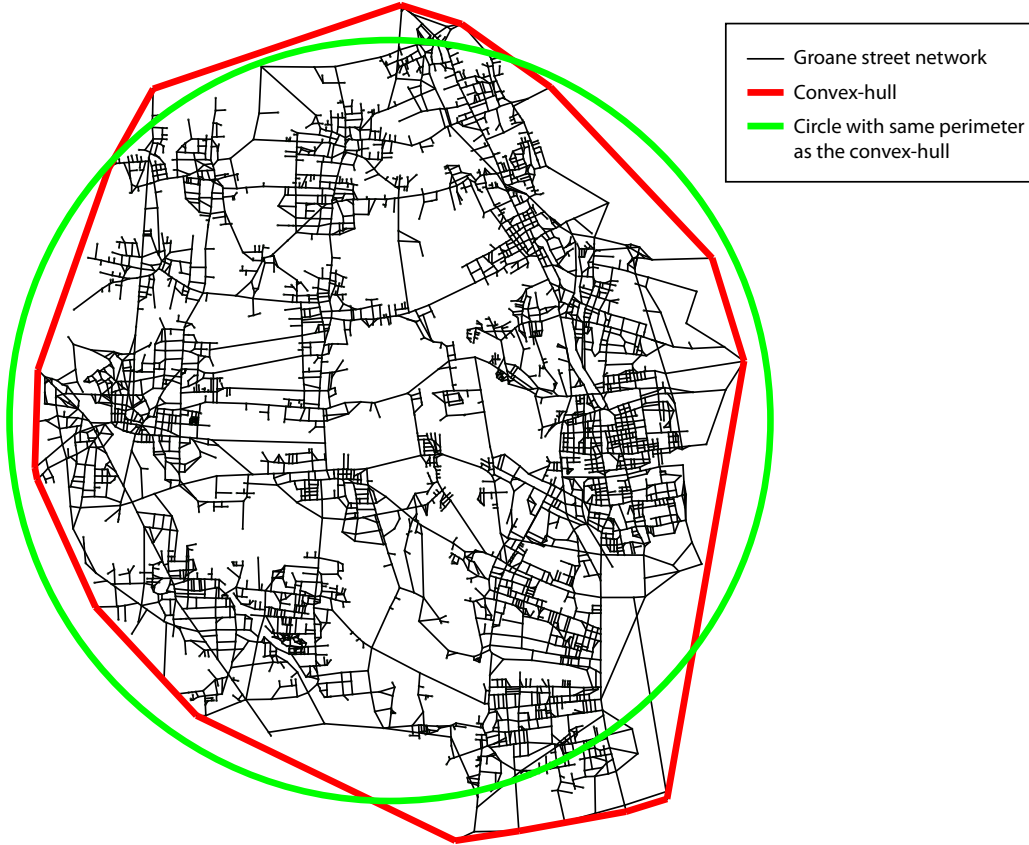
FIG. S1. *Method used to calculate the relative radius of 2D geographical network.* Related to Figure 2. The street network of Groane is shown in black and its convex-hull polygon is shown in red. The green circle has the same perimeter as the network convex-hull. The value of the average edge length of Groane street network used in Figure 2N is normalized by the radius of the green circle shown here. The same procedure was performed for all the other 2D geographical networks shown in Figure 2N.
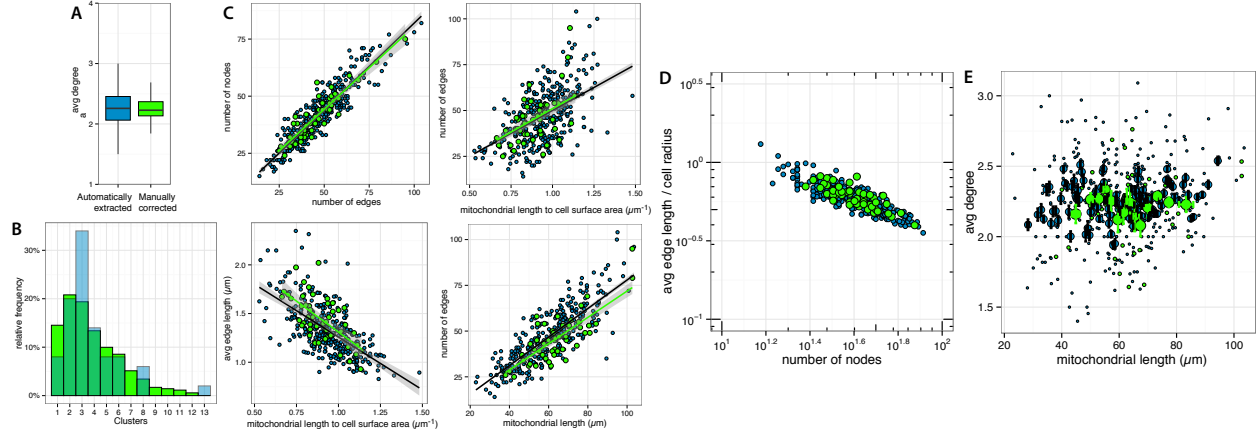
FIG. S2. *Automatically extracted wild-type mitochondrial networks are similar to their manually corrected counterparts.* Related to Table 1. We used blue and green to represent automatically extracted and manually corrected networks, respectively. **(A)** Average degree defined as the average number of edges attached to a node. **(B)** Relative frequency of connected components for both datasets. **(C)** Topological and geometrical attributes for both datasets. Solid lines correspond to the best fitting and the gray area represent the 95% CI of the mean. **(D)** Scaling between average edge length and number of nodes for both datasets. **(E)** Average degree as a function of mitochondrial total edge length for both datasets. Small dots represent the raw data and big dots represent the rolling average. Error bars represent the 95% CI of the mean. The good agreement between the automatically extracted and manually corrected data suggests that the networks automatically generated by MitoGraph are similar to the manually corrected networks.
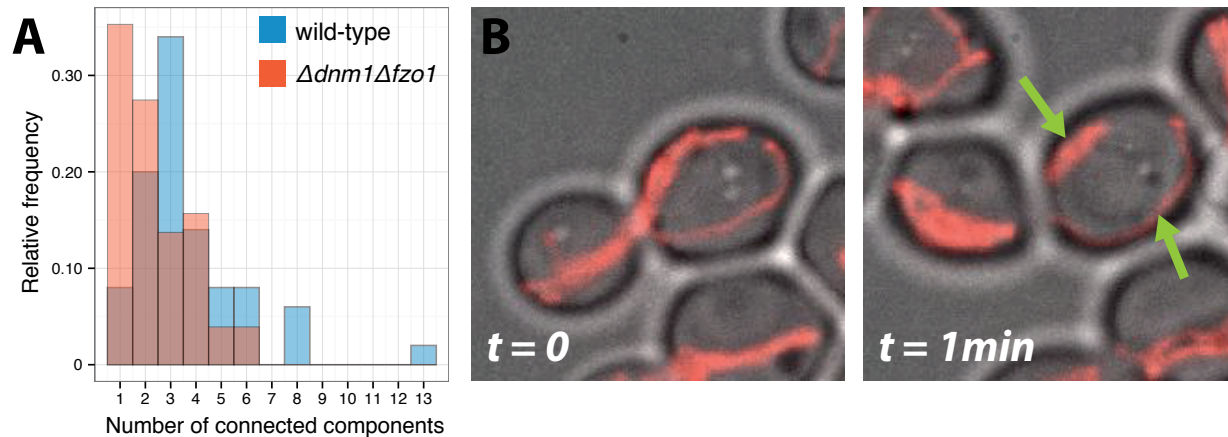
FIG. S3. *Cytokinesis is capable of splitting mitochondrial tubules in two even in absence of fusion and fission dynamics.* Related to Table 1. **(A)** Distribution of number of connected components in mitochondrial networks of wild-type (blue) and $\Delta dnm1\Delta fzo1$ cells. **(B)** Time-points of a $\Delta dnm1\Delta fzo1$ cell before and after division. Mitochondria are shown in red and overlaid with bright field MIP. The continuous mitochondrial tubule at t=0 is broken apart by the cytokinesis after 1 min. The mother cell ends up having two disconnected mitochondrial tubules as indicated by the green arrows.
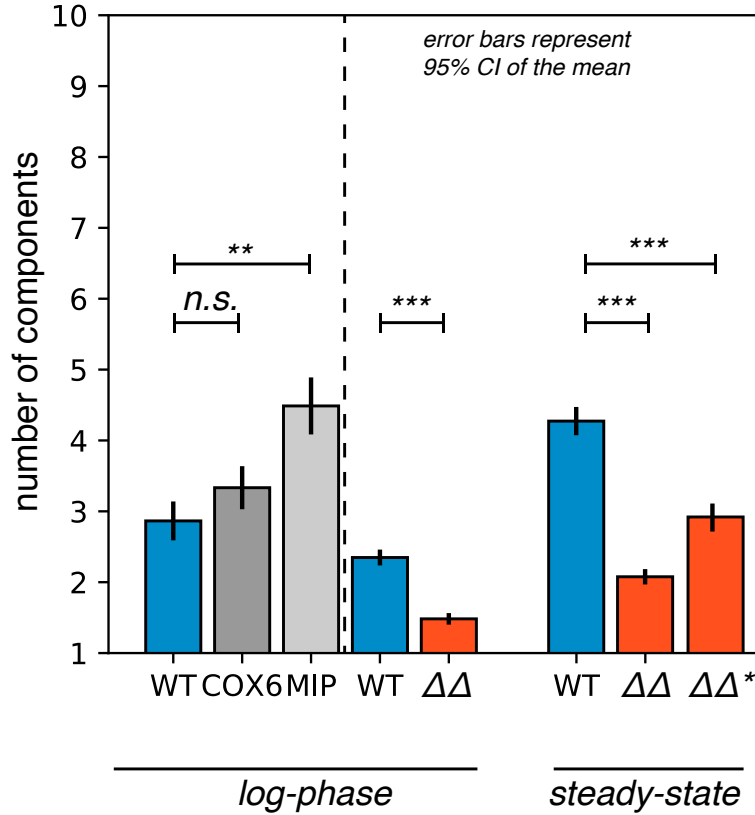
FIG. S4. *Mutants with defective respiratory function or lack of mtDNA generate mitochondrial networks with more connected components.* Related to Table 1. The average number of connected components in wild-type (WT) yeast cells (blue, N=111, 56, and 351 cells, respectively) and mutant yeast cells from matched experiments. $\Delta\Delta$ represents $\Delta dnm1\Delta fzo1$ cells in red (N=89, 260 and 51 cells, respectively; $\Delta\Delta*$ are the manually corrected set of networks used in the main results section), while COX6 and MIP represent $\Delta cox6$ (rho-; N=39) and Δmip (rho0; N=39) cells, in two shades of gray respectively. Statistical comparison was performed with Wilcoxon rank sum with Bonferroni adjustment for pairwise comparison.
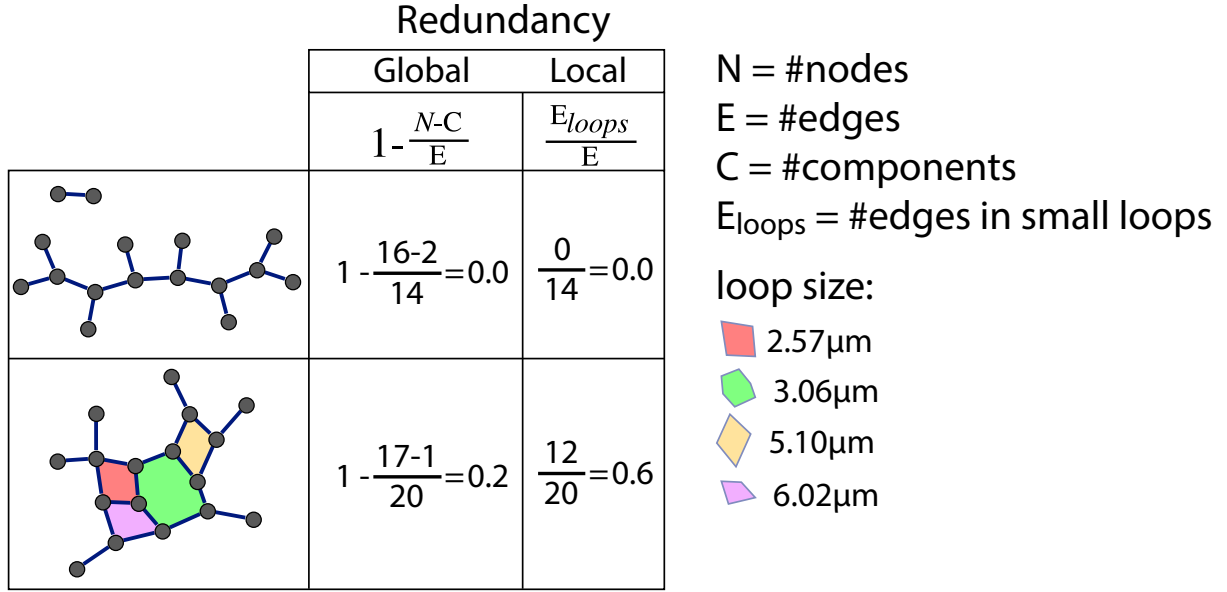
Redundancy

	Global	Local
	$1-\frac{N\text{-}C}{E}$	$\frac{E_{loops}}{E}$
(network with no loops)	$1-\frac{16\text{-}2}{14}=0.0$	$\frac{0}{14}=0.0$
(network with loops)	$1-\frac{17\text{-}1}{20}=0.2$	$\frac{12}{20}=0.6$

N = #nodes
E = #edges
C = #components
E_{loops} = #edges in small loops

loop size:
- 2.57µm
- 3.06µm
- 5.10µm
- 6.02µm

FIG. S5. *Measurements of global and local redundancy* applied to two examples of networks (see methods). Related to Figure 2. The first example corresponds to the middle $\Delta dnm1\Delta fzo1$ network shown in Figure 2I, which displays no loops. Therefore, both global and local redundancy are zero. The second example corresponds to a region of the bottom wild-type network shown in Figure 2H. The network displays four loops, three of which fall in the category of small size loops (loops with length in the range 2µm-6µm). Global and local redundancy values of this network are 0.2 and 0.6, respectively. Networks are shown in topological view, which means that size of loops do not correspond to the real values shown on the right side.
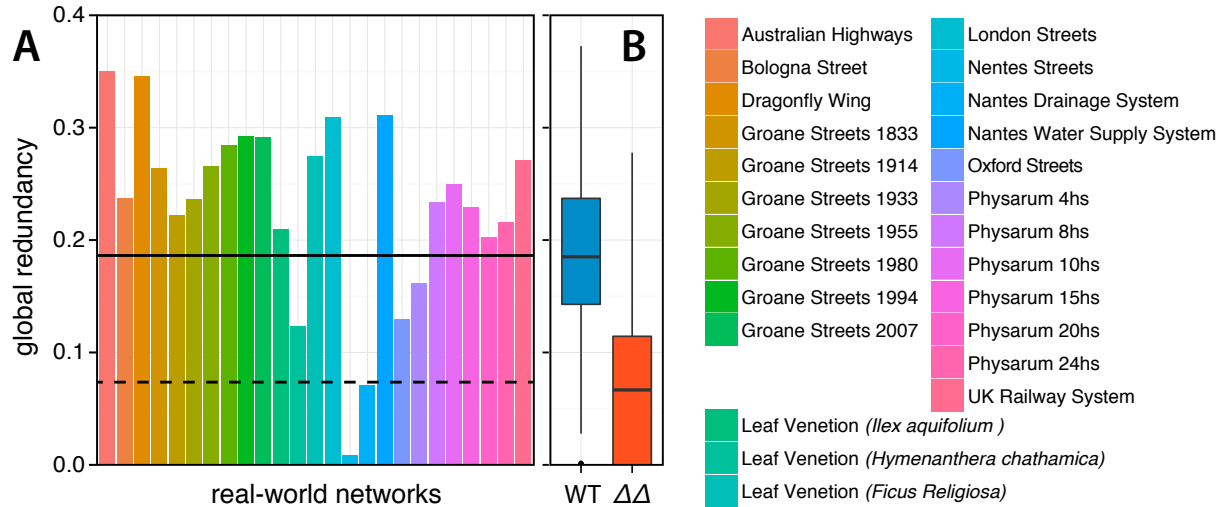
FIG. S6. *Mitochondrial networks have decreased global redundancy in the absence of fission and fusion.* Related to Figure 2. **(A)** The bars represent the global redundancy of some examples of real-world networks. The solid/dashed black line represents the global redundancy of wild-type and $\Delta dnm1 \Delta fzo1$ mitochondrial networks, respectively. **(B)** Global redundancy for wild-type and dnm1fzo1 mutant cells. The box plots represent the median and the 25th and 75th percentile. The vertical lines represent the data range.

9
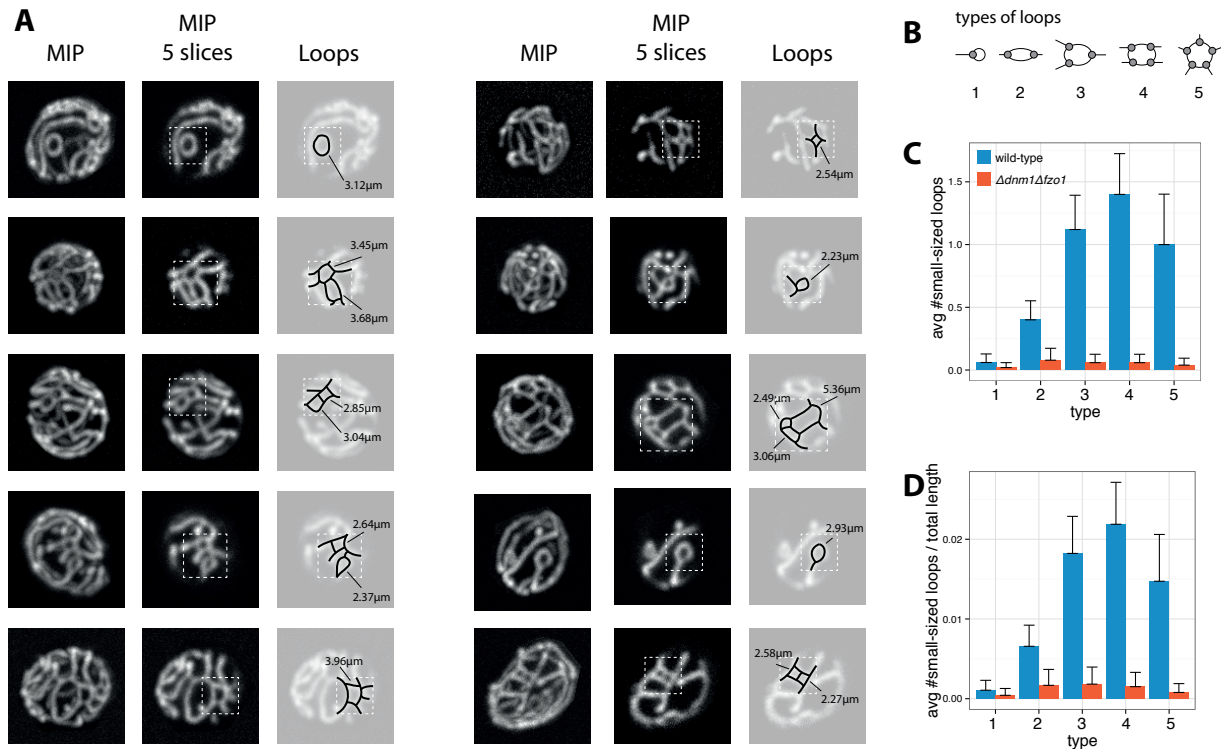
FIG. S7. *Small-sized loops are absent in mitochondrial networks of fission/fusion defective cells.* Related to Figure 2. **(A)** Examples of small sized loops in wild-type mitochondrial networks. First and second columns represent the maximum intensity projection (full cell and 5 slices, respectively). Third column highlights the small-sized loops for which the perimeter is in between 2μm and 6μm. **(B)** Different types of loops found in mitochondrial networks based on their number of sides, i.e. number of edges that form the loop. **(C)** Average number of small-sized loops found in wild-type and mutant cells. **(D)** Average number of loops normalized by the total length of the network. Error bars represent the 95% CI of the mean.
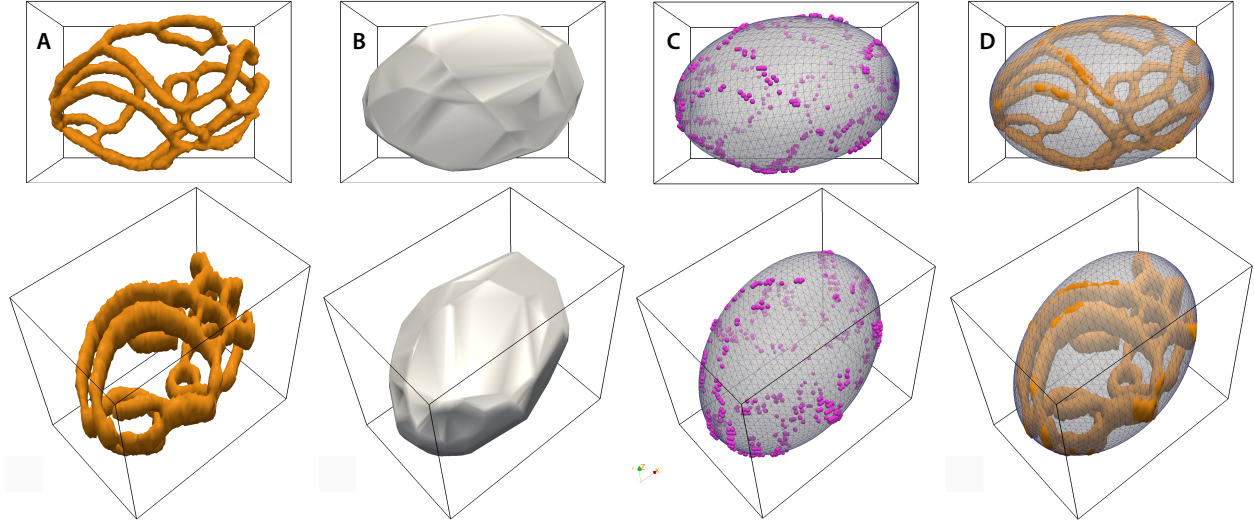
FIG. S8. *Method for estimation of cell surface.* Related to Figure 2. **(A)** We start with an experimental mitochondrial surface provided by MitoGraph; **(B)** We calculate the corresponding convex-hull of the 3D mitochondrial surface; **(C)** The convex-hull points are used to fit a 3D ellipsoid using the least squares algorithm described in MATLAB Central file ID #24693. **(D)** Original mitochondrial surface and the resulting ellipsoid.
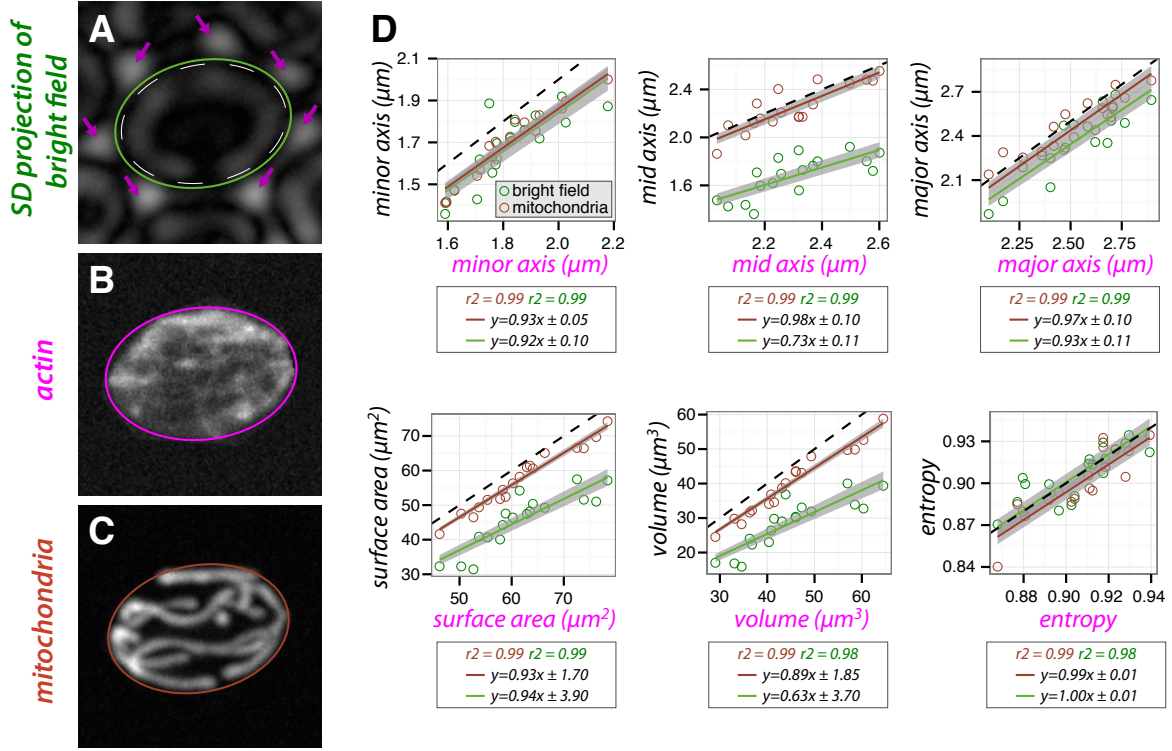
FIG. S9. *Different methods are used to validate the cell surface detection.* Related to Figures 1 and 2. **(A)** Standard deviation projection of bright field z-stack of a yeast cell containing labels for both mitochondria and actin. The internal bright ring and the bright spots indicated by purple arrows are used as reference for the manual traces of cell surface represented by the solid green line. **(B)** MIP of the actin-labeled cell shown in (A). The solid purple line indicates the cell surface determine by the convex-hull method based on the actin signal. **(C)** MIP of the mitochondria-labeled cell shown in (A). The solid brown line represents the cell surface determined by the convex-hull method based on the mitochondria signal. **(D)** Relevant properties of the resulting ellipsoid geometry obtained by both methods: manual tracing (green dots) and mitochondria-based convex-hull (brown dots) compared to the ground truth (actin-based convex-hull). Dashed black lines represent the identity $y = x$ (a perfect method should have all dots lying on this line). The solid brown and green lines represent the best fitting and the gray area represent the 95% CI of the mean.
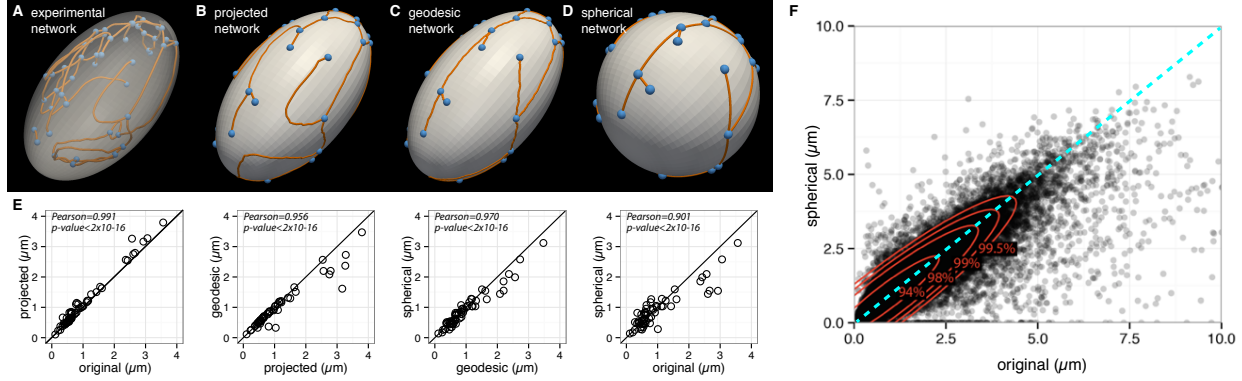
FIG. S10. *Process of mitochondrial network projection onto a spherical surface.* Related to Figures 1, 2, and 3. **(A)** We start with an experimental mitochondrial network and the ellipsoid that represents the cell surface. **(B)** The skeleton is projected onto the ellipsoid surface by assigning each point of the skeleton to the closest point of the ellipsoid meshwork. **(C)** The edges of projected network are converted in geodesic paths between respective nodes along the ellipsoidal geometry. **(D)** The geodesic network from (C) is projected onto the surface of a sphere with the same surface area as the initial ellipsoid. **(E)** The length of edges (N=45, one point per edge) at each step of the process of generating the spherical projection. The solid black line represents the reference $y = x$. **(F)** Heat map representing the length of edges (N=195593) in the spherical representation versus the original length for all the cells used in this study. Red solid lines represent the contours that contain 94%, 98%, 99% and 99.5% of black points. Cyan dashed line represents the identity $y = x$.
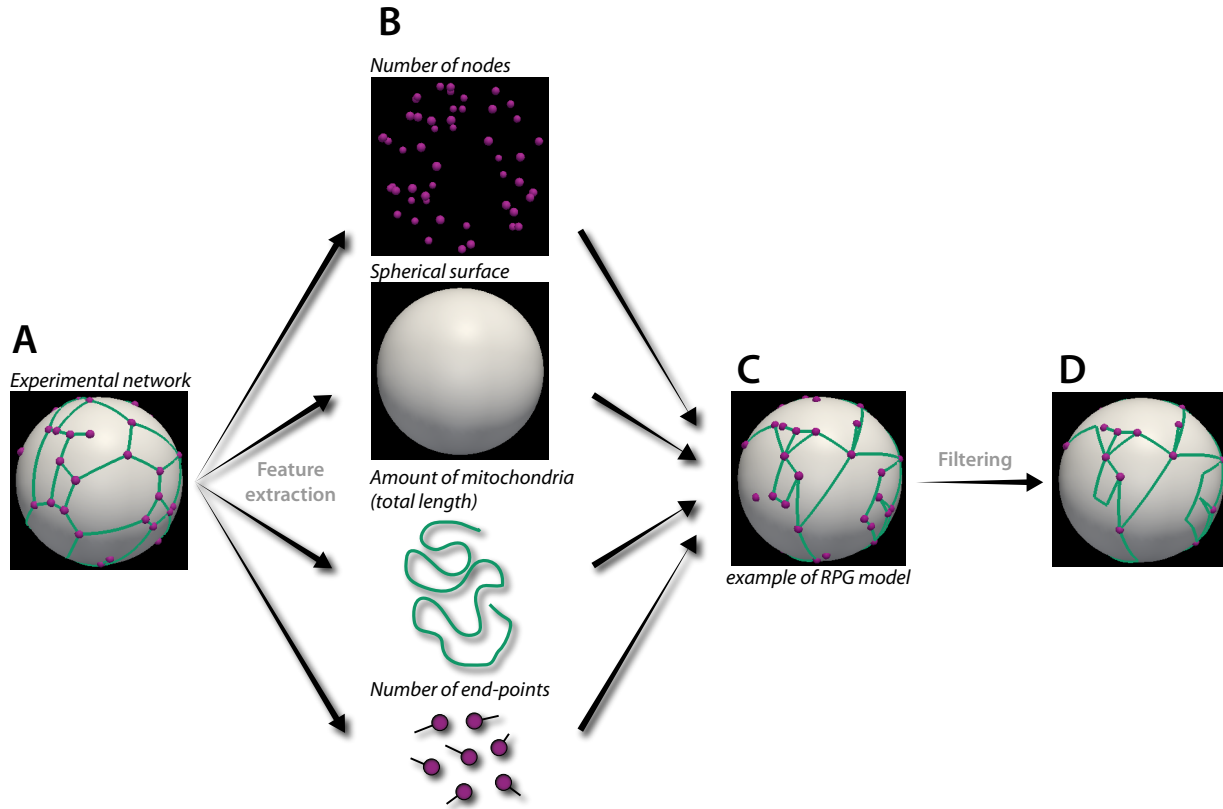
FIG. S11. *Random planar geographical (RPG) model to simulated random instances of mitochon-drial networks.* Related to Figure 2. **(A)** We start with the spherical representation of a given mitochondrial network; **(B)** We extract the number of nodes, spherical surface area, amount of mitochondria and fraction of nodes with degree 1 from this representation; **(C)** The attributes are used to generate a random instance of the RPG model; **(D)** The resulting network is filtered to ensure that the final network does not display nodes with degree 0 or 2.